August 2019

Investigation of Dielectrophoretic Microfluidic Trap System for Separation and Parallel Analysis of Single Particles

Tae Joon Kwak
University of Wisconsin-Milwaukee

INVESTIGATION OF DIELECTROPHORETIC MICROFLUIDIC TRAP SYSTEM FOR SEPARATION AND PARALLEL ANALYSIS OF SINGLE PARTICLES

by

Tae Joon Kwak

A Dissertation Submitted in

Partial Fulfillment of the

Requirements for the Degree of

Doctor of Philosophy
in Engineering

at

The University of Wisconsin-Milwaukee

August 2019

ABSTRACT

INVESTIGATION OF DIELECTROPHORETIC MICROFLUIDIC TRAP SYSTEM FOR SEPARATION AND PARALLEL ANALYSIS OF SINGLE PARTICLES

by

Tae Joon Kwak

The University of Wisconsin-Milwaukee, 2019
Under the Supervision of Professor Woo-Jin Chang

Separation and identification of single molecules and particles based on their chemical, biochemical and physical properties are critical in wide range of biomedical applications. Manipulating a single biomolecule requires sensitive approaches to avoid damage to the molecule. Recent progress in micro- and nano-technology enabled the development of various novel methods and devices to trap, separate, and characterize micro- and nano-particles. In this dissertation, a microfluidic particle trap system to electrically separate particles at the single particle level was developed through particle manipulation methods using dielectrophoresis. The research in this dissertation will explain the operation strategy and setup of the novel dielectrophoretic trap system to separate and analyze single particle. The characteristics of the various shapes and sizes of traps were investigated experimentally and theoretically for single molecules and particles trapping.

To
my parents,
my wife,
and
my children

TABLE OF CONTENTS

LIST OF FIGURES

LIST OF TABLES

LIST OF ABBREVIATIONS

3D	Three-dimensional
AC	Alternating current
CAD	Computer aided design
CCD	Charge-coupled device
CM	Clausius-Mossotti
CVD	Chemical vapor deposition
DC	Direct current
DEP	Dielectrophoresis
DI	Deionized
FEA	Finite element analysis
HMDS	Hexamethyldisilazane
ITO	Indium-tin-oxide
MEMS	Micro-electro-mechanical-systems
n-DEP	Negative dielectrophoresis
p-DEP	Positive dielectrophoresis
PET	Polyethylene terephthalate
PR	Photoresist
PSF	Point spread function
PTFE	Polytetrafluoroethylene
RGB	Red-green-blue
RPM	Revolutions per minute
SEM	Scanning electron microscope
UV	Ultra violet

Chapter 1

Introduction

1.1 Particle trapping and separation

The ability to separate and manipulate biological particles based on their physical and biochemical properties enables a wide range of biomedical applications, for example disease diagnosis, genetic analysis, and drug screening [1, 2]. Biological sample mixtures are commonly separated through a series of bio-separation processes such as centrifugation [3], filtration [4], chromatography [5], density gradient methods [6], and a variety of methods has been studied over the past several decades. However, fractionating small amounts of bioparticles from other co-existing particles that have similar chemical and physical properties in the solution is still challenging [7].

Recently, lab-on-a-chip type devices have attracted interest for the fractionation of bioparticles because they require small amounts of samples and enable faster separation, higher sensitivity and selectivity, and have the capability to integrate multiple treatments. Various separation mechanisms have been adopted for the microfluidic lab-on-a-chip separation of bioparticles, such as affinity-based antibody-coated surfaces [8, 9] and paper-fluidic devices [10], trapping using ciliated micropillars [11], sieving by physical size [12], and acoustic filtering [13].

Manipulating a single biomolecule requires very sensitive approaches to avoid damage to the molecules. A variety of methods such as optical, microfluidic, mechanical, magnetic, and electrical fields were used in controlling micro- and nano-particles in particle trapping, focusing, separating and characterizing applications. In general, methods that use electrical fields are suitable for bioparticle manipulation due to the benefits of strong controllability, ease of operation, high efficiency and slight damage to targets as shown in **Error! Reference source not found.** [14]. Recent advancements in micro- and nano-technology using electrical fields enabled the development of various novel methods and devices including gel electrophoresis [15], capillary

electrophoresis [16, 17], and dielectrophoresis [18], to trap, separate, and characterize micro- and nanoparticles.

Table 1. Comparison of different particle control methods [14].

Methods	***Controllability***	***Operation***	***Efficiency***	***Cost***	***Damage***
Optical	*Strong*	*Hard*	*Low*	*High*	*Slight*
Microfluidic	*Weak*	*Easy*	*High*	*Low*	*Little*
Mechanical	*Strong*	*Hard*	*Low*	*Low*	*Large*
Magnetic	*Strong*	*Hard*	*Low*	*Low*	*Slight*
Electrical fields	*Strong*	*Easy*	*High*	*Low*	*Slight*

1.2 Dielectrophoresis (DEP)

When a dielectric particle is exposed to a non-uniform electric field, the particle is polarized by the electric field and the particle experience a force along the electrical field gradient. This phenomenon is called dielectrophoresis (DEP) as proposed by Herbert Pohl [19]. The magnitude and direction of the DEP force is determined by the relative polarizabilities of the particle and of the surrounding medium. For a homogeneous sphere of radius r, the DEP force is calculated by using an equation:

$$F_{DEP} = 2\pi r^3 \varepsilon_0 \varepsilon_m Re[K(\omega)] \nabla \left|\vec{E}_{rms}\right|^2 \quad (1)$$

where ε_0 and ε_m are the permittivity of the free space and medium, *E* is the applied electric field, and $K(\omega)$ denotes the Clausius-Mossotti (CM) factor which contains all the frequency

dependence and the components of the complex dielectric constant of the DEP force. The Clausius-Mossotti factor is expressed as:

$$\mathrm{K}(\omega) = \frac{\varepsilon_p^* - \varepsilon_m^*}{\varepsilon_p^* + 2\varepsilon_m^*} \tag{2}$$

Here, the indices *p* and *m* denote the particle and the surrounding medium, respectively. When an alternating electric field with angular frequency of ω is applied, the complex dielectric permittivity is defined by:

$$\varepsilon^* = \varepsilon - j\frac{\sigma}{\omega} \tag{3}$$

where the σ is the electrical conductivity and the j is the imaginary number unit.

Direction of the DEP force is determined by the real part of the CM factor ($Re[K(\omega)]$). When the complex permittivity of the particle ε_p^* is higher than that of the surrounding medium ε_m^*, resulting $Re[K(\omega)] > 0$, and then the particle will displace itself towards the higher electric field region. This is positive dielectrophoresis (p-DEP) as shown in Figure 1 left. On the other hand, when the complex permittivity of the ε_p^* is lower than the that of the particle, resulting $Re[K(\omega)] < 0$, the dipoles localized in the surrounding medium will move the particle towards the minimum of the electric field region [20]. This is negative dielectrophoresis (n-DEP) as shown in Figure 1 right. The values of CM factor are restricted by the limits of $-0.5 < Re[K(\omega)] < 1$ for spherical particles depending on the frequency of the applied electric field and the relative magnitudes of ε_p^* and ε_m^* [21].

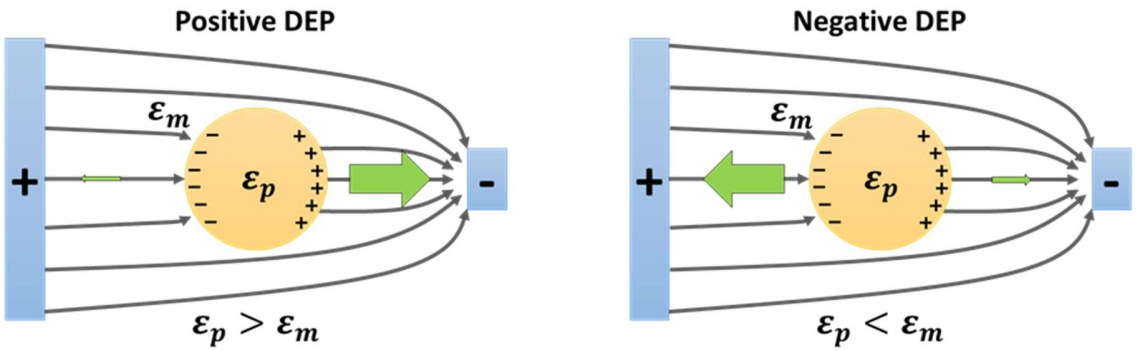

Figure 1. Illustration of positive DEP (left) and negative DEP (right) for a dipole induced charged particle.

If the particle is consisted of more than one substance, the conductivity and permittivity of each layer should be considered to determine permittivity. Thus, for studies on biological particles with heterogeneous configurations, such as micro-organisms, cells, and particles that have multiple components, more complex consideration is needed to be analyzed. Conventionally, the "single-shell model [22]" which combines the layers into an effective conductivity and permittivity is used to estimate the permittivity of the heterogeneous particles as shown in Figure 2 using following equation :

$$\varepsilon^*_{p(eff)} = \varepsilon^*_{outer} \frac{\frac{r^3_{outer}}{r^3_{inner}} + 2\frac{\varepsilon^*_{inner} - \varepsilon^*_{outer}}{\varepsilon^*_{inner} + 2\varepsilon^*_{outer}}}{\frac{r^3_{outer}}{r^3_{inner}} - \frac{\varepsilon^*_{inner} - \varepsilon^*_{outer}}{\varepsilon^*_{inner} + 2\varepsilon^*_{outer}}} \tag{4}$$

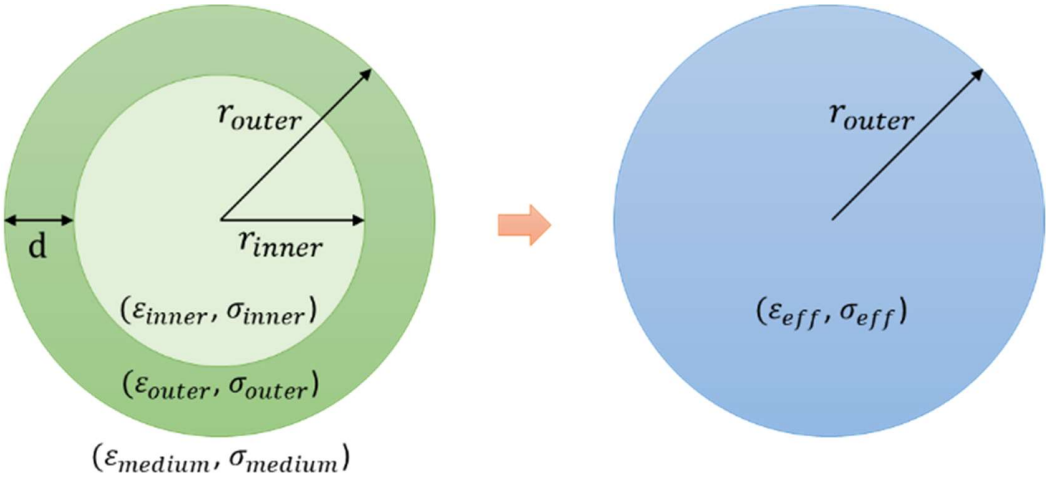

Figure 2. Schematic of single-shell modeling of a heterogeneous particle with respect to the dielectrophoretic (DEP) properties.

1.3 Electrode design for single particle trap

In general, interdigitated electrodes (IDE) are used for particle separation and manipulation in dielectrophoresis researches [18, 23]. In the IDE based devices, particle separation and manipulation have performed utilizing the characteristics that the electric field gradient is higher at the electrode edges compared to the center of the electrodes and the gap between the electrodes. Particles move to the edge of the IDE when p-DEP applied, on the other hand, the particles move to the center of the IDE or gap between the IDE when n-DEP applied as shown in Figure 3. The particle manipulation with IDE based system is suitable for manipulating large number of particles; however, it is not optimized for single particle level studies. Moreover, the location of particles following the length of the IDE electrode system cannot be predictable, because of the even and parallel distribution of the force between electrodes. When an electrical potential is applied to an electrode, the magnitude of the electric field is strongest at the edge of the electrode and decreases by the distance from the edge. Especially in n-DEP, it is easier to predict the position of particles

in the vertical direction because the electric field in the vertical direction is strong enough to hold the particles on both sides. However, in the lateral direction, the highest electric field is generated from the edge of the electrode and the size of the electric field decreases along the length of the electrode, so the particles can move due to the reduced stiffness in the lateral direction.

The closed-form electrodes, such as circular and square shapes as shown in Figure 4 and Figure 5, have been considered as appropriate structures for trapping particles with DEP since they are easy to predict the trapped position of the particles, especially in n-DEP [24–26]. When an electric potential is applied to an electrode, the electric field is highest at the edge of the electrode and becomes smaller as it is farther from the edge of the electrode. Therefore, in the case of n-DEP in these closed-form electrodes, each edge of the electrode is located at a uniform distance from the lowest electric field area in the center of the electrode, so the particles move away from the electrode edge towards the center of the trap shape. This makes easier to predict where the particles are trapped. In this dissertation, therefore, the closed-form electrodes are proposed as electrode design for single particle trap.

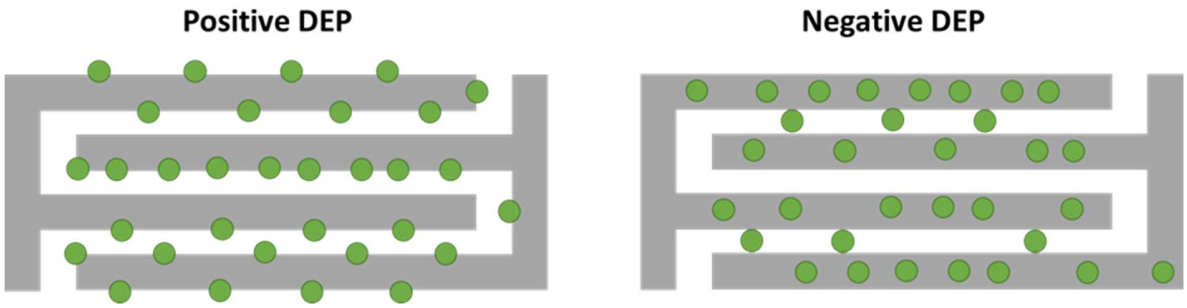

Figure 3. Dielectrophoretic behavior of particles in IDE devices.

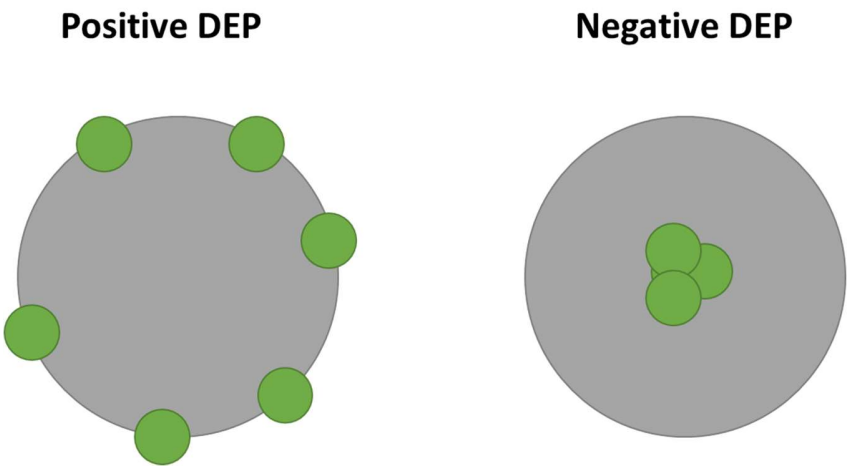

Figure 4. Dielectrophoretic behavior of particles in circular closed-form trap devices.

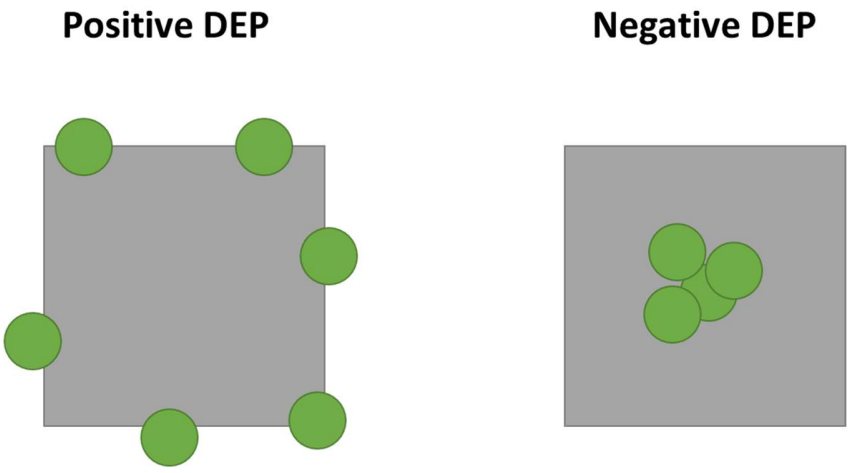

Figure 5. Dielectrophoretic behavior of particles in square closed-form trap devices.

1.4 Scope of the dissertation

The goal of this dissertation is to develop a novel microfluidic particle trap system using dielectrophoresis to electrically trap, separate, and analyze single molecules and particles. Figure 6 illustrates the concept of the dielectrophoretic microfluidic corral trap system. Each chapter of the dissertation addresses various components for determining the characteristics of a novel microfluidic particle trap system using dielectrophoresis.

Chapter 1 provides an overview of particle trapping and separation techniques, as well as an introduction of dielectrophoresis.

Chapter 2 presents the method of numerical simulation and geometrical analysis of the dielectrophoretic microfluidic trap. Numerical simulation analysis for trapping particles with various shapes of traps, and behavior of particles according to trap shapes are presented.

Chapter 3 describes the fabrication and experimental setup of dielectrophoretic microfluidic trap device.

Chapter 4. describes experimental methods for particles trapping and separation by the dielectrophoretic microfluidic trap system. The trapping particles with various sizes of microchannels, trapping various sizes of particles, and separation of particles are described.

Chapter 5 provides a conclusion, as well as addresses recommendations for future work.

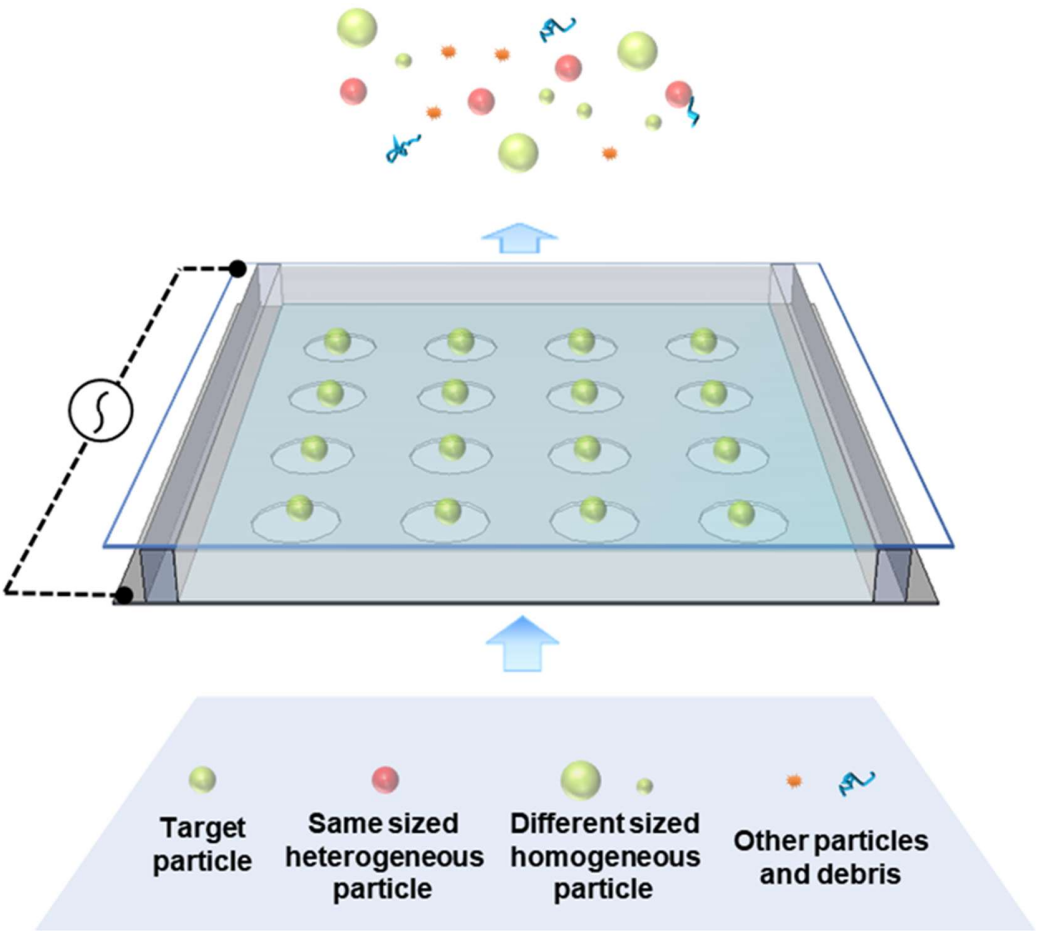

Figure 6. Concept of the dielectrophoretic microfluidic corral trap system.

Chapter 2

Numerical study of the Shape Characteristics of the Dielectrophoretic Microfluidic Trap Devices

2.1 Overview

The DEP can be used to separate, sort, manipulate and transport bioparticles, based on their dielectric properties and the DEP force is directly related to the spatial gradient of the electric field. The spatial gradient of the electric field varies depending on the geometry of the dielectrophoretic trapping device. By changing their geometrical structure, the trap could have different electric force fields in the trapping region. The behavior of the particle trapping is depending on the direction and the magnitude of the DEP forces near the trap. For effective particle trapping, the trapping force needs to overcome the kinetic energy and the drag force of the particles when the particles are in motion.

In this chapter, numerical study by finite element analysis (FEA) method examines the effect of different trap geometries on particle trapping using DEP forces. The results were used to determine the optimum trap shape for the particle trap system. Numerical analysis of the force field in circular, square, and triangular shaped particle traps and behavior of particles in the force field are discussed.

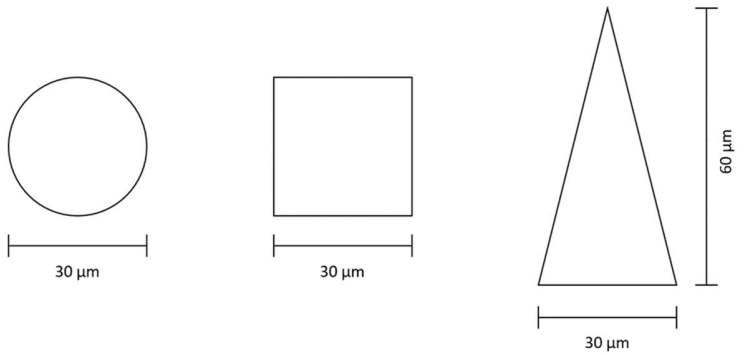

Figure 7. Circle, square, and triangle in which the characteristics of trapping are analyzed through numerical analysis.

2.2 Physics and governing equation

The introduction of appropriate physics and governing equations into numerical analysis systems are the most important factors when numerically analyzing a system. To theoretically confirm whether the DEP force is formed around the microstructure electrodes and can focus the particles in the trap, the numerical simulation analysis of the DEP force vectors distribution had to be obtained. I simulated the magnitude and vector distributions of the DEP force in the DEP trap system using FEA method using COMSOL Multiphysics (V5.2, COMSOL Inc, Sweden) with AC/DC module. To derive a DEP force acting on a particle from the electric field, the governing DEP Equation (1) for each x, y, and z component is solved as follows:

$$2 * \mathrm{pi} * ((\varepsilon_o)[\mathrm{F/m}]) * ((\varepsilon_m)) * ((\mathrm{r[m]})\hat{}3) * \mathrm{Re[K(\omega)]} * (2 * \mathrm{es.Ex} * \mathrm{d(es.Ex, x)} + 2 * \mathrm{es.Ey} * \mathrm{d(es.Ey, x)} + 2 * \mathrm{es.Ez} * \mathrm{d(es.Ez, x)}) \quad (5)$$

$$2 * \mathrm{pi} * ((\varepsilon_o)[\mathrm{F/m}]) * ((\varepsilon_m)) * ((\mathrm{r[m]})\hat{}3) * \mathrm{Re[K(\omega)]} * (2 * \mathrm{es.Ex} * \mathrm{d(es.Ex, y)} + 2 * \mathrm{es.Ey} * \mathrm{d(es.Ey, y)} + 2 * \mathrm{es.Ez} * \mathrm{d(es.Ez, y)}) \quad (6)$$

$$2 * \mathrm{pi} * ((\varepsilon_o)[\mathrm{F/m}]) * ((\varepsilon_m)) * ((\mathrm{r[m]})\hat{}3) * \mathrm{Re[K(\omega)]} * (2 * \mathrm{es.Ex} * \mathrm{d(es.Ex, z)} + 2 * \mathrm{es.Ey} * \mathrm{d(es.Ey, z)} + 2 * \mathrm{es.Ez} * \mathrm{d(es.Ez, z)}) \quad (7)$$

The parameters used in this study were determined assuming that 2 μm radius polystyrene particle is suspended in DI water. The permittivity of the free space, ε_o, was 8.854×10^{-12} and the relative permittivity of the medium, ε_m, was 80.1 [18, 25]. The real part of the Clausius-Mossotti factor *Re[K(ω)]* was -0.4602 at 1 MHz, 0.9937 at 1 kHz, and the conductivity of the medium, i.e. DI water, was 2 - 4 μS /cm [18, 25].

2.3 Geometry and boundary conditions

In order to characterize the traps for the immobilization of particles in the trap device, simplified geometries of each circular, square, and triangular shape with pairs of periodic condition on wall interfaces were used for the numerical analysis. Figure 8 illustrates the geometry and boundary conditions for the circular trap with diameter of 30 μm. Figure 9 illustrates the geometry and boundary conditions for the square trap with 30 μm of each side. Figure 10 illustrates the geometry and boundary conditions for the triangular trap with base of 30 μm and height of 60 μm. Each trap has a 100 nm thick chromium electrode with a circular, square, triangular shape at the surface, with an ITO counter electrode located at a distance of 30 μm. The water between the two electrodes is filled as a medium.

Three materials used in the devices were chromium, water, and ITO. Properties of the materials for the numerical simulation were determined based on the default material properties in COMSOL Multiphysics database except for relative permittivity. The values of the relative permittivity of chromium, water, and ITO used in the numerical study were 12, 80.1, and 3.3378, respectively, which are obtained from previous studies [18, 25, 26].

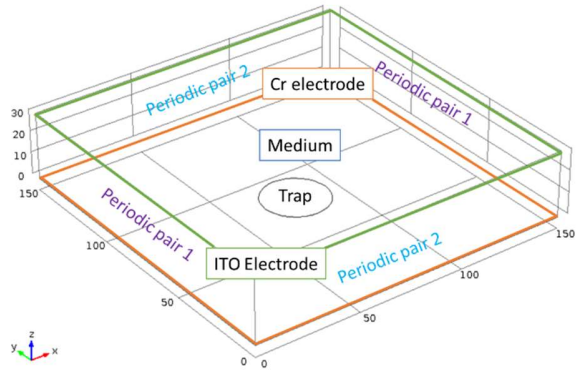

Figure 8. Circular trap geometry and boundary conditions for the numerical analysis.

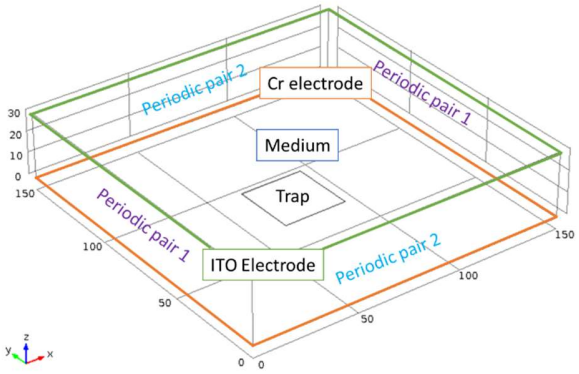

Figure 9. Square trap geometry and boundary conditions for the numerical analysis.

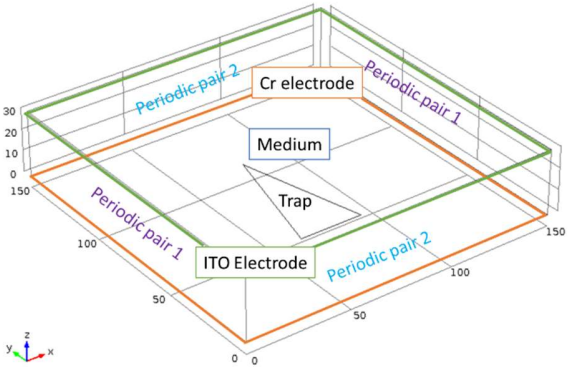

Figure 10. Triangular trap geometry and boundary conditions for the numerical analysis.

2.4 Mesh

In order to obtain a reliable resolution of the numerical simulation study, mesh optimization is one of the most important factors. The circular, square, and triangular particle traps analyzed in this study were all set to physics-controlled extremely fine tetrahedral meshes. Especially, the size of mesh was initially set to be less than 200 nm around and inside of the trap, where displacement of the particle position is important, and this approach has been proven to be reliable in microscale observations from our previous work [18].

In order to increase the accuracy of the simulation analysis, the resolution of each derived graph has been adjusted from standard resolution to additional fine resolution in post-processing, so the spacing between each date value in the graph is smaller. The smaller element spacings allow finer resolution of the analysis. In addition, since the distance of the mesh elements are different from each other, the data set is interpolated at intervals of 10 nm in order to obtain a uniform interval resolution in the numerical analysis according to the particle positions.

Figure 11 shows the mesh for the circular trap with 17.1×10^6 elements and 3.41×10^6 degree of freedom. Figure 12 shows the mesh for the square trap with 17.1×10^6 elements and 3.42×10^6 degree of freedom. Figure 13 shows the mesh for the triangular trap with 17.1×10^6 elements and 3.42×10^6 degree of freedom.

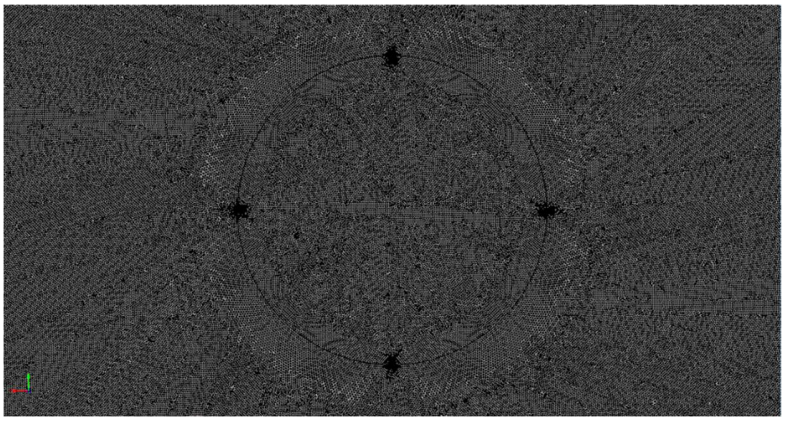

Figure 11. The circular trap with meshes.

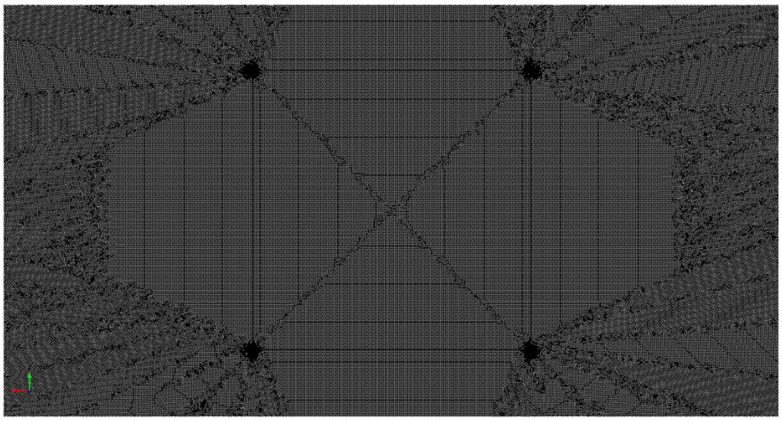

Figure 12. The square trap with meshes.

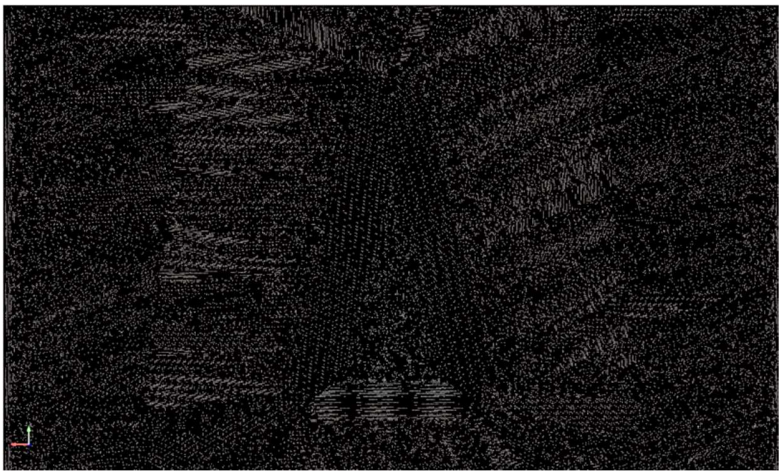

Figure 13. The triangular trap with meshes.

2.5 Simulated DEP forces on traps

2.5.1 Electric field and direction of DEP forces on each trap

In each trap shape, I examined the direction of the DEP force that affects particles when the particles are around the trap. Figure 14, Figure 15, and Figure 16 present the simulated electric field (surface color) and direction and relative magnitude of p-DEP and n-DEP forces (red arrows) around each circular, square, and triangular trap. An AC 100 kHz 8 $V_{peak\text{-}to\text{-}peak}$ is applied to simulate the effect of the p-DEP and an AC 1 MHz 8 $V_{peak\text{-}to\text{-}peak}$ is applied to simulate the effect of the n-DEP to the electrodes.

Each size and direction of the arrows represents the p-DEP and n-DEP forces that affects a particle when a 2 μm radius particle is located at the position indicated by the arrow. The length of arrows is set to the logarithm; thus, the length of each arrow indicates the relative strength of the DEP force formed at the location.

Since the electric field gradient is stronger at the edge of the trap and is lower at the inside of the trap, the particle will be pulled toward the edge of the trap in the case of p-DEP, and will be pushed toward the inside of the trap in the case of n-DEP. Since the real number of the CM factor is higher in p-DEP than the n-DEP, the magnitude of the p-DEP forces is higher than n-DEP forces. However, the n-DEP forces formed from all directions will immobilize the particle at a certain place in the trap, this makes easy to predict the trapped position of the particles. Especially in the triangular trap, since the shape of the trap is not symmetric in x-axis, the direction of the DEP force is not symmetric as well. Characteristics of the geometrical effects of DEP will be discussed in more detail in the next section with a numerical graph form.

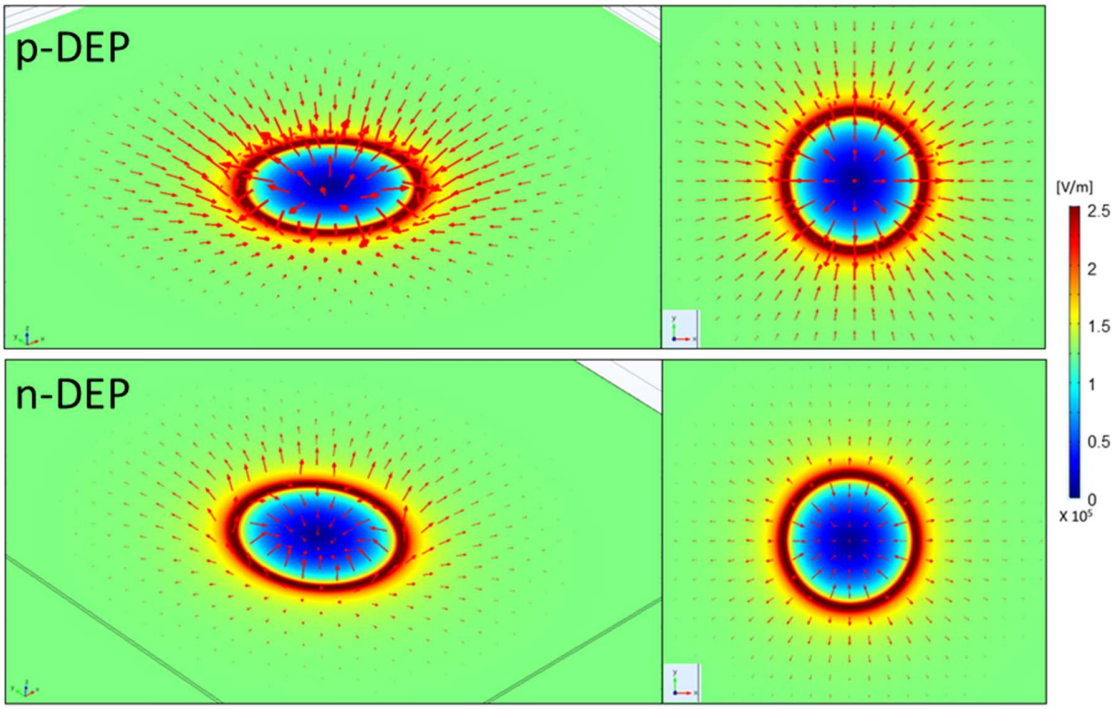

Figure 14. Normalized electric field and direction of the p-DEP and n-DEP forces in a circular trap.

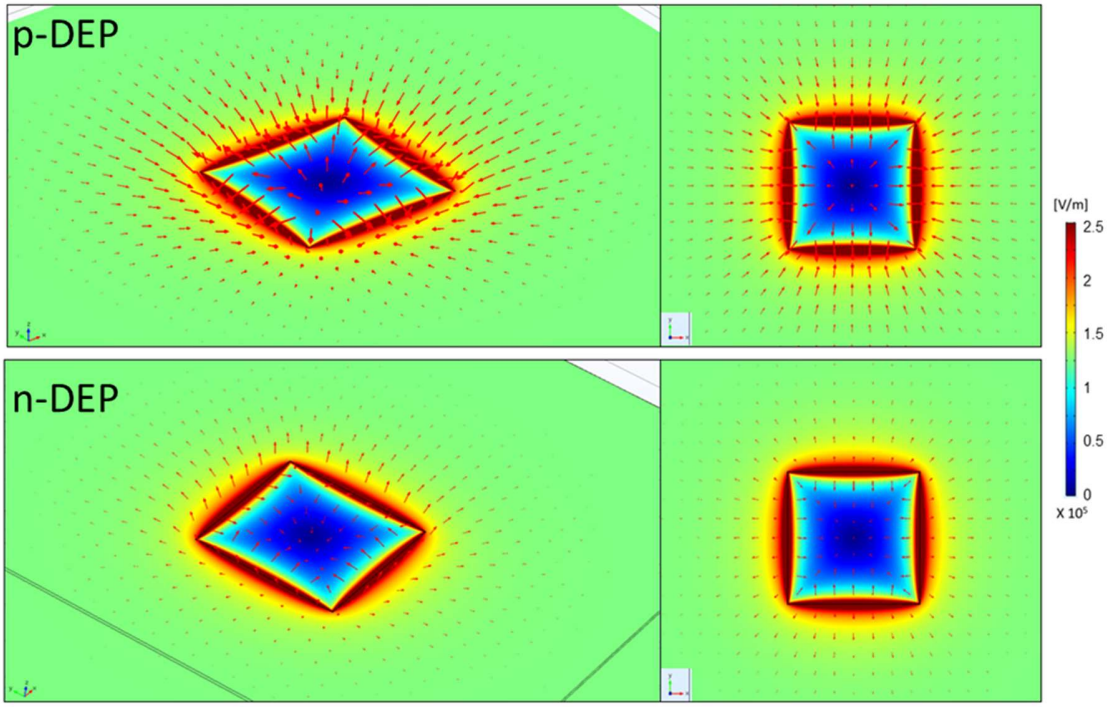

Figure 15. Normalized electric field and direction of the p-DEP and n-DEP forces in a square trap.

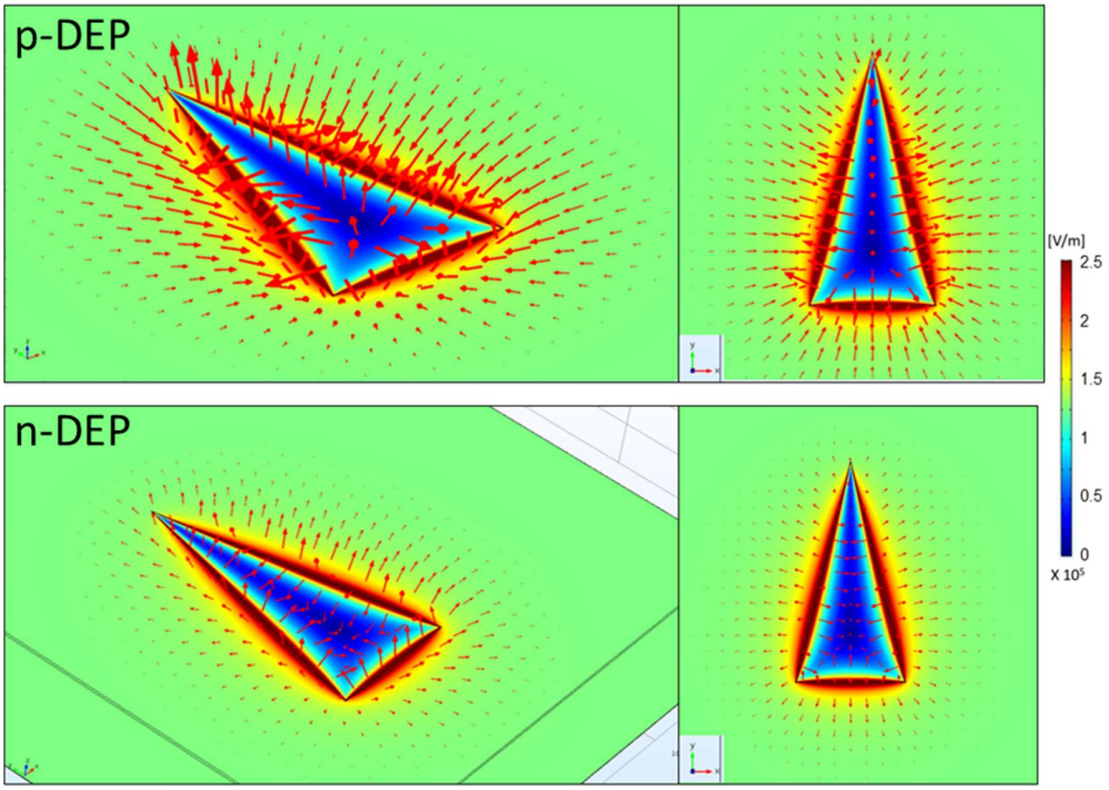

Figure 16. Normalized electric field and directions of the p-DEP and n-DEP forces in a triangular trap.

2.5.2 Cross-sectional view of the DEP forces

Figure 17, Figure 18, and Figure 19 show the cross-sectional view of the electric field and directions of the p-DEP and n-DEP forces on each circular, square, and triangle traps. The position of the cross-section in each trap is indicated by a red line. In the cross-section view, the formation of the electric field and direction of the p-DEP and n-DEP forces can be viewed two-dimensionally. In general, the electric field is strongest at the electrode edge and weakest within the trap.

Since the formation of the DEP force varies depending on the gradient of this electric field, the direction of the p-DEP force forms a vortex from the inside of the trap where the weaker electric

field, to the edge of the electrode where the stronger electric field. On the contrary, the direction of the n-DEP force forms a vortex from the edge of the trap where the stronger electric field, to the center of the electrode where the weaker electric field. Between two edges of the circular and square trap, all n-DEP forces are directed towards the center of the trap. In other words, the particle inside the trap receives a repulsive force towards the bottom center of the trap when an electric potential is applied to the circular and square trap electrodes. In the case of the triangular trap, the difference in the electric field gradient is relatively smaller because the length of the Y-axis is longer than that of the circular and square traps. Also, the shape is not symmetrical in both directions. Therefore, the DEP forces in the Y-axis direction are relatively smaller to the center of the trap, and the formation of the DEP forces is not symmetrical.

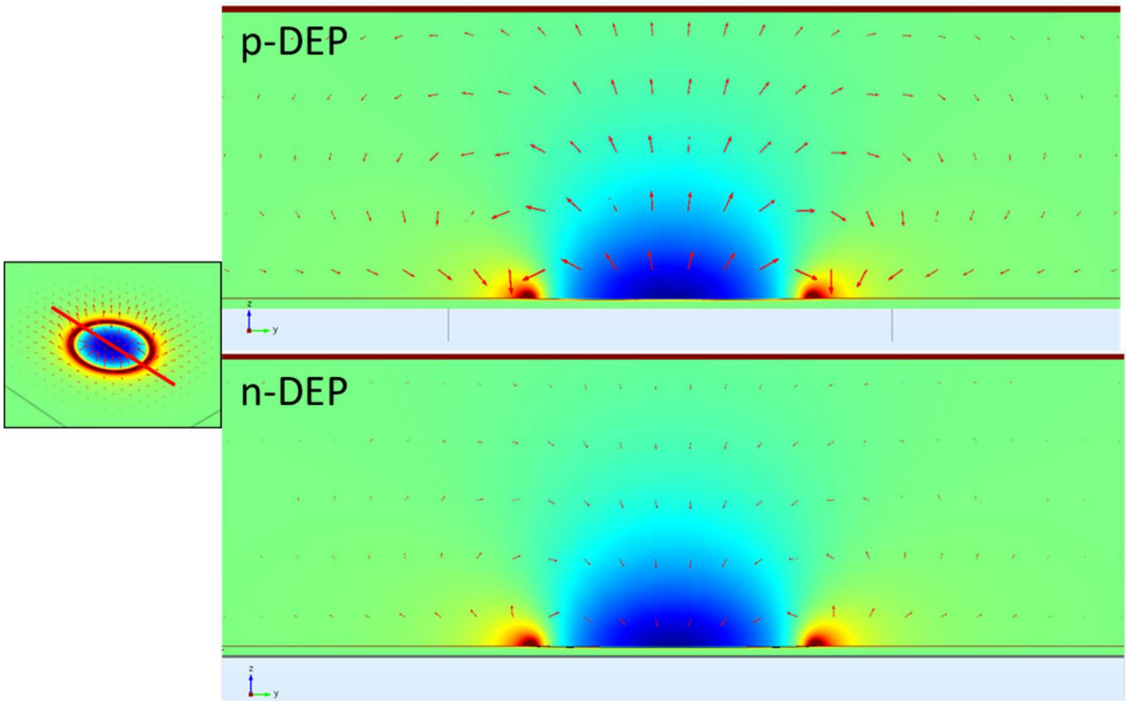

Figure 17. Cross-sectional view of the electric field and directions of the DEP forces on circular trap.

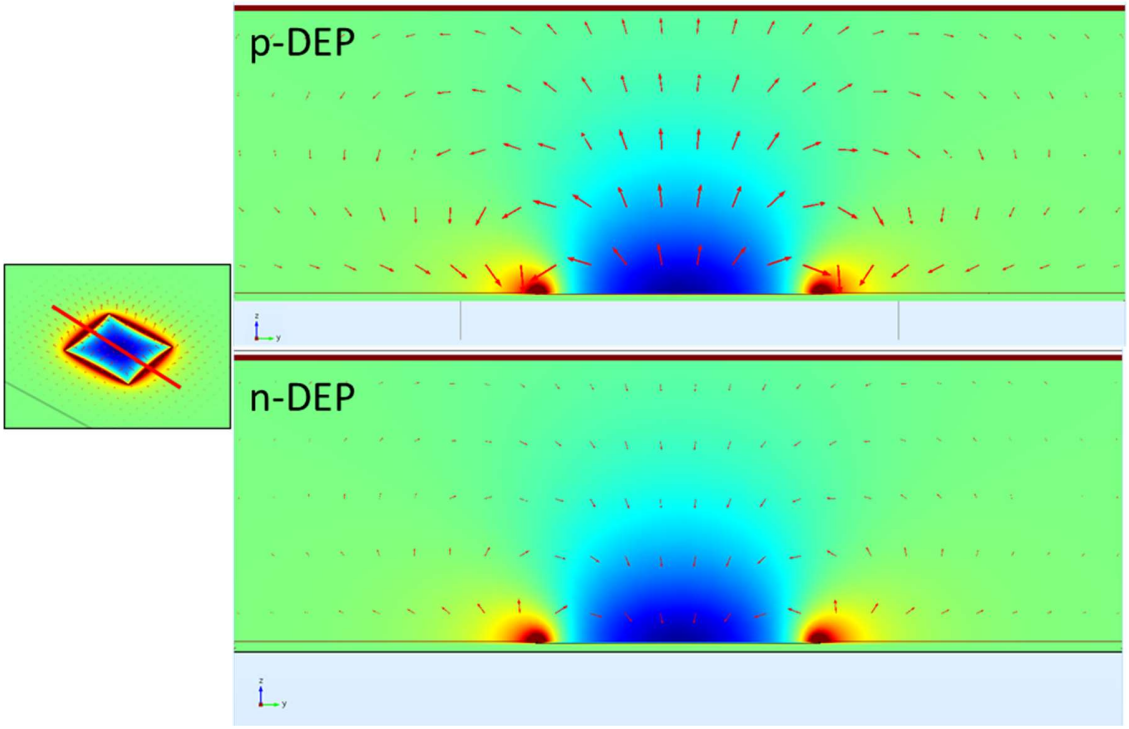

Figure 18. Cross-sectional view of the electric field and directions of the DEP forces on square trap.

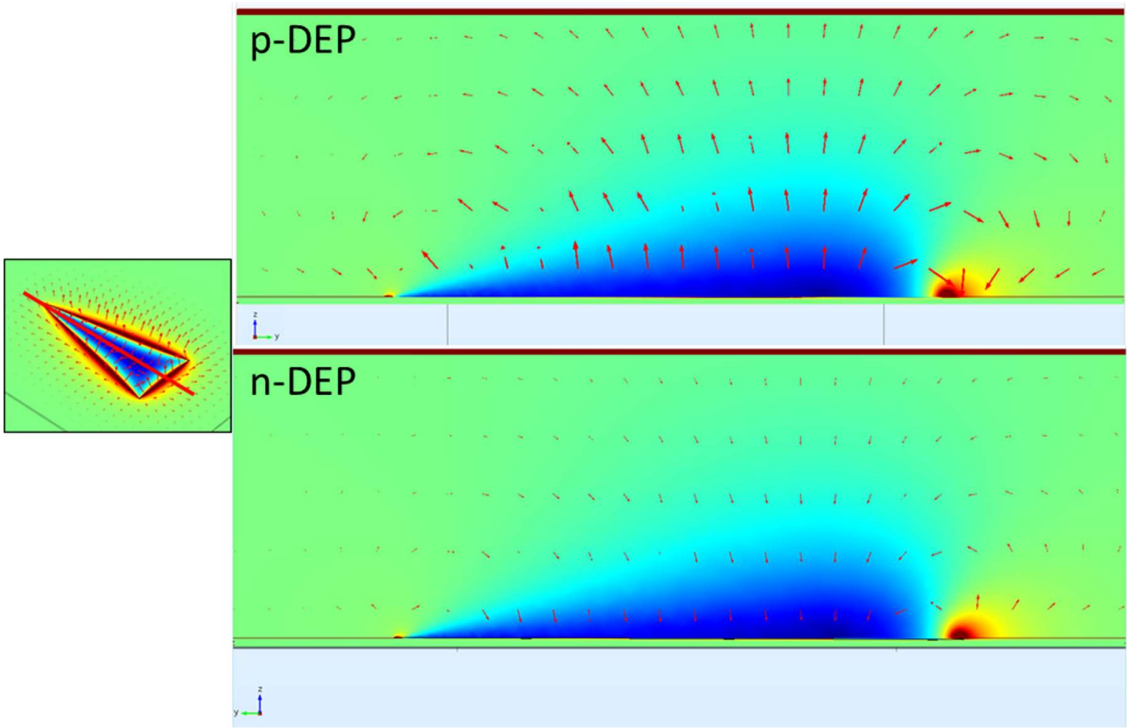

Figure 19. Cross-sectional view of the electric field and directions of the DEP forces on triangular trap.

2.5.3 DEP force magnitude on axis for each trap

Figure 20, Figure 21, and Figure 22 show the line graph of DEP forces in each X, Y, and Z -axis for circular, square, and triangular traps to quantify and to compare the magnitude of the DEP forces more thoroughly. The yellow trap shapes in each graph were inserted to display the location of the traps. Since the cut lines for each trap were set along the X-axis penetrates the center of the traps as shown in each inset, components of the X-axis DEP forces were negligible due to the symmetric characteristic of the trap shapes. The Y-axis DEP forces for each trap refer to the magnitude of the force directed to the right of the graph. Thus, the negative Y-axis DEP force value after the 50 μm point, i.e. the center of each trap, is the magnitude of the DEP force directed to the left of the graph. For the Z-axis DEP force of each graph, the positive values indicate the upward Z-axis DEP forces, and the negative values indicate the downward Z-axis DEP forces.

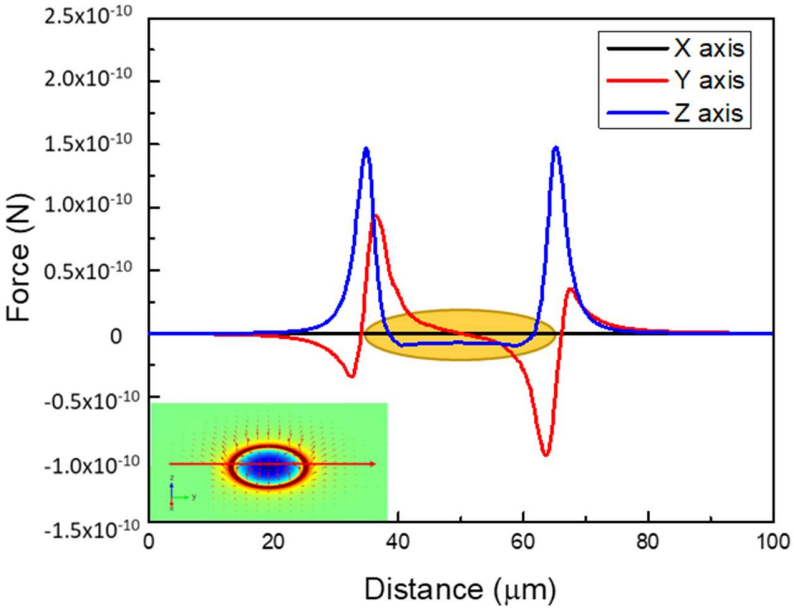

Figure 20. Line graph of DEP forces in each axis for a circular trap.

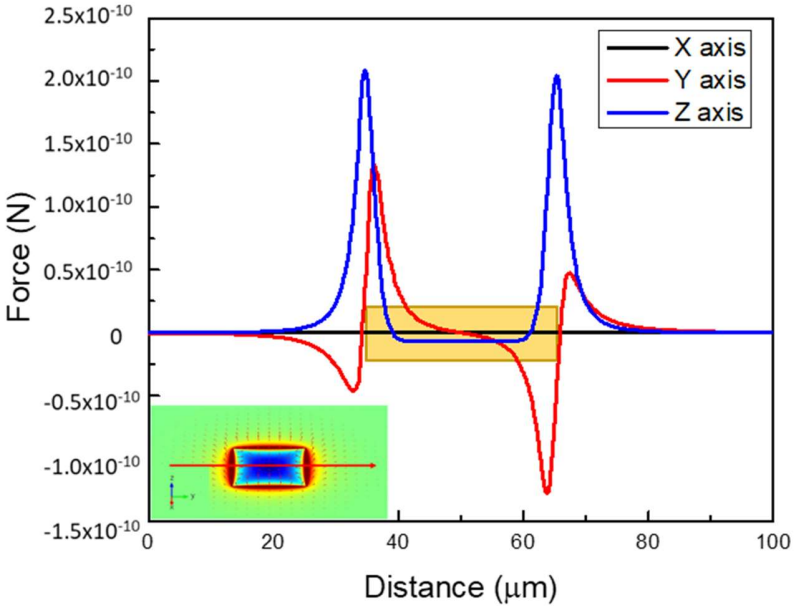

Figure 21. Line graph of DEP forces in each axis for a square trap.

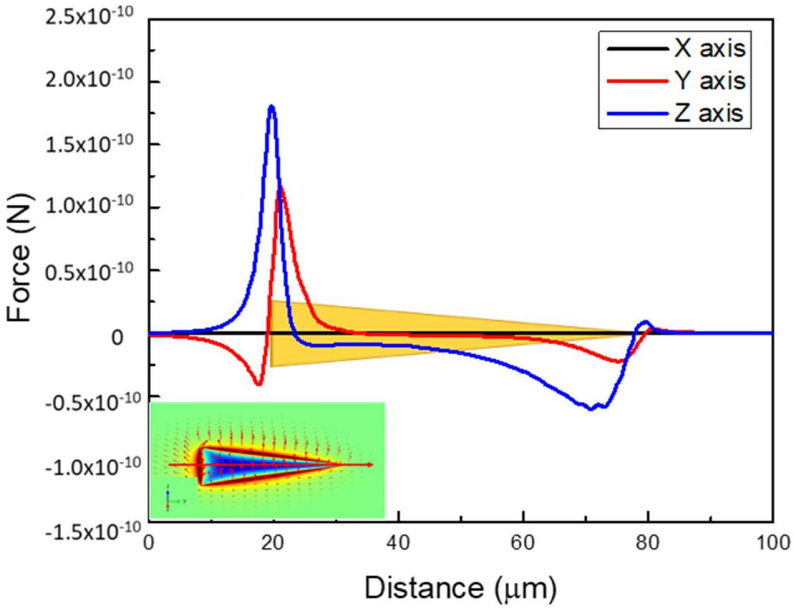

Figure 22. Line graph of DEP forces in each axis for a triangular trap.

2.5.4 Trapping force comparison for the circular and square trap

For Y-axis DEP forces of each graph, negative values indicate the Y-axis DEP force acting in the left direction (origin of the arrow) of the schematic, and positive values indicate the Y-axis DEP force acting in the right direction (tip of the arrow) of the schematic. The Y-axis DEP force acts to reduce or increase the movement of particles in the channel, and the balance of the Y-axis DEP forces hold particles trapped within the trap in place.

For the Y-axis DEP forces of the circular trap and square trap in Figure 20 and Figure 21, the DEP forces inside of the trap acts toward the center of the trap, while the DEP forces outside of the trap pushed the particle out of the trap. In general, the DEP forces inside the trap are stronger than the repulsive forces on the outside of the trap. The maximum repulsive DEP forces pushing out the particle from the outside of the circular trap and the square trap were calculated as 3.43×10^{-11} N and 4.68×10^{-11} N, and the force pushing the particle inside the circular trap and the square trap toward the trap center were calculated as 9.32×10^{-11} N and 1.34×10^{-10} N, respectively. Comparing the trapping DEP forces of Y-axis on the circular trap and the square trap, the square trap was analyzed to be up to 36% stronger in outside and up to 43% larger in inside than the circular trap.

For Z-axis DEP forces of each graph, negative values represent downward Z-axis DEP forces closer to the electrode glass slide, and positive values represent upward Z-axis DEP forces. The downward Z-axis DEP force is added to the gravity, and thus pulling the floating particles in the channel toward the surface of the trap and holding the trapped particles on the bottom of the trap.

For the Z-axis DEP forces of the circular trap and square trap in Figure 20 and Figure 21, the DEP forces near the outside edge of the trap are directed upward, and the DEP forces inside of

the trap are directed downward. The maximum downward Z-axis DEP forces of the circular trap and square trap were calculated as 9.45×10^{-12} N and 6.98×10^{-12} N, respectively. Comparing the trapping DEP forces in the Z-axis inside the traps for circular trap and square trap, the circular traps were analyzed to be up to 35% stronger than the square traps.

In addition, the DEP forces at 45 degrees diagonal across the X and Y axes of the circular and square traps were analyzed in Figure 23 and Figure 24 to compare geometrical characteristic between circular trap and square trap. Since the circular trap is symmetric about the X- or Y-axis of all angles, diagonal axis analysis showed the same pattern as the DEP force in Figure 20 for the Y-and Z-axis for the DEP force on the circular trap. However, in the case of a square trap, the diagonal length is increased as 42.43 μm because the one side of the square is multiplied by the square root of 2, which is about 1.41 times greater than the length of one side. Since the increased distance reduces the magnitude of the electric field and the electric field gradients at the vertex of the rectangle are significantly smaller, the diagonal DEP forces in the square trap are relatively weaker than axial DEP forces. As in a square trap, the trapping force varies along the direction, the stiffness can be reduced. The stiffness is the force to hold the particles after trapping because the trapped particles can move toward the weaker force direction.

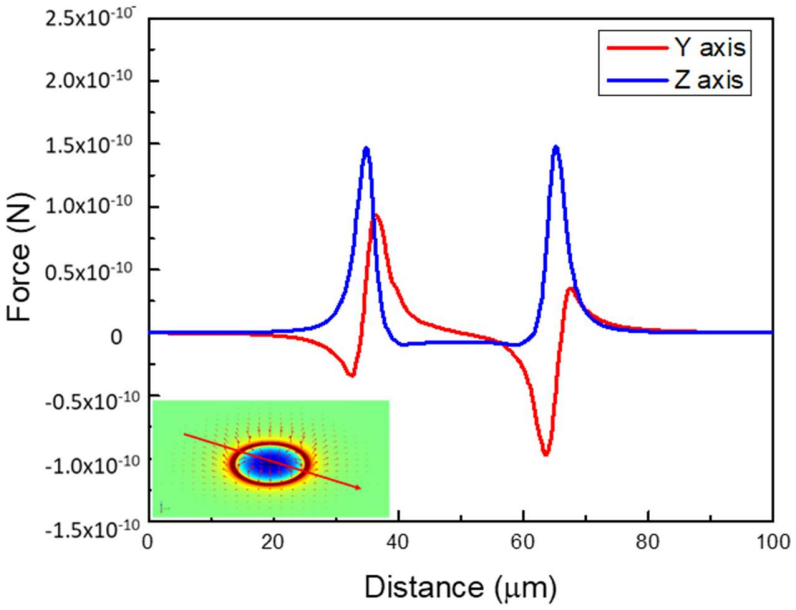

Figure 23. Diagonal line graph of DEP forces in Y and Z axis for a circular trap.

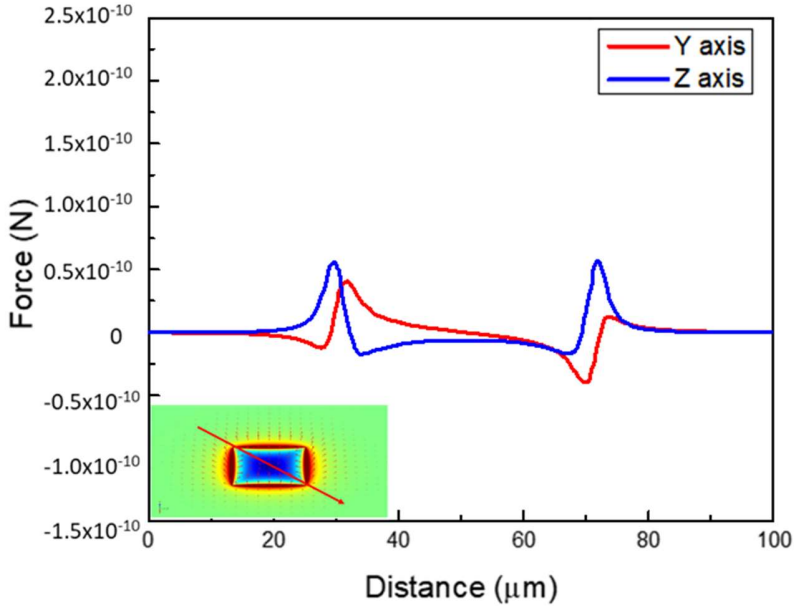

Figure 24. Diagonal line graph of DEP forces in Y and Z axis for a square trap.

2.5.5 Trapping force for the triangular trap

In the case of a triangular trap, the Y-axis of the DEP forces on the right side and on the left side are different because the trap shape is not symmetrical about the perpendicular to the axis being analyzed in Figure 22. For the base side of the triangular trap (left in the graph), the maximum repulsive DEP forces pushing out the particle from the outside of the trap was 4.03×10^{-11} N, and the force pushing the particle inside the trap toward the trap center was 1.17×10^{-10} N. For the vertex side of the triangular trap (right in the graph), the maximum repulsive DEP forces pushing out the particle from the outside of the trap was 2.23×10^{-11} N, and the force pushing the particle inside the trap toward the trap center was 3.38×10^{-12} N. Therefore, if a particle in the channel is trapped while moving from the base side of the triangle toward the vertex, the particle can be pulled toward the trap surface by the strong downward Z-axis force, however, the Y-axis trapping force at the vertex side is relatively weak, so the particle can easily escape from the trap. On the other hand, when a particle moves from the vertex side to the base side of the triangular trap, it may be difficult to penetrate the center of the vertex and enter the trap because of the repulsive force around the vertex can make the particle bypass the trap due to the repulsive force to the outside around vertex. Once a particle is trapped inside the trap, it can be held by the Y-axis forces acting on the base side of the trap, however, the trapping force of the Y-axis acting on the vertex side is relatively small so that the particle can travel along the Y-axis in the trap due to reduced stiffness.

2.6 Determining the appropriate trap shape

In this chapter, I have numerically analyzed circular, square, and triangular traps to evaluate the availability of dielectrophoretic single particle trapping. The triangular trap was evaluated to have a relatively strong downward trapping force due to the gradually narrowing geometry, but asymmetric shape could cause particle loss. The square trap has relatively strong lateral trapping forces, but diagonal trapping forces are relatively smaller than axial forces, so that this can cause the stiffness reduction.

Overall, the circular trap was evaluated to have uniform n-DEP trapping forces in all directions, with appropriate lateral and downward n-DEP trapping force magnitudes. Moreover, the circular trap was evaluated to have robust stiffness, which is expected to have a great advantage in analyzing captured bio-particles.

Chapter 3

Fabrication and Experimental Setup of the Dielectrophoretic Microfluidic Trap Devices

3.1 Overview

This chapter focuses on the experimental methods, materials, and equipment for the dielectrophoretic microfluidic trap system. The photolithographic fabrication process and the experimental setup for the dielectrophoretic trap devices are discussed in detail.

3.2 Fabrication methods of DEP trap device

The microfluidic chip device used in this study was fabricated through photolithographic and metal deposition technique which is a well-known manufacturing process of Micro Electro Mechanical Systems (MEMS) as shown in Figure 25 [25]. The detailed fabrication process is described in each subsection.

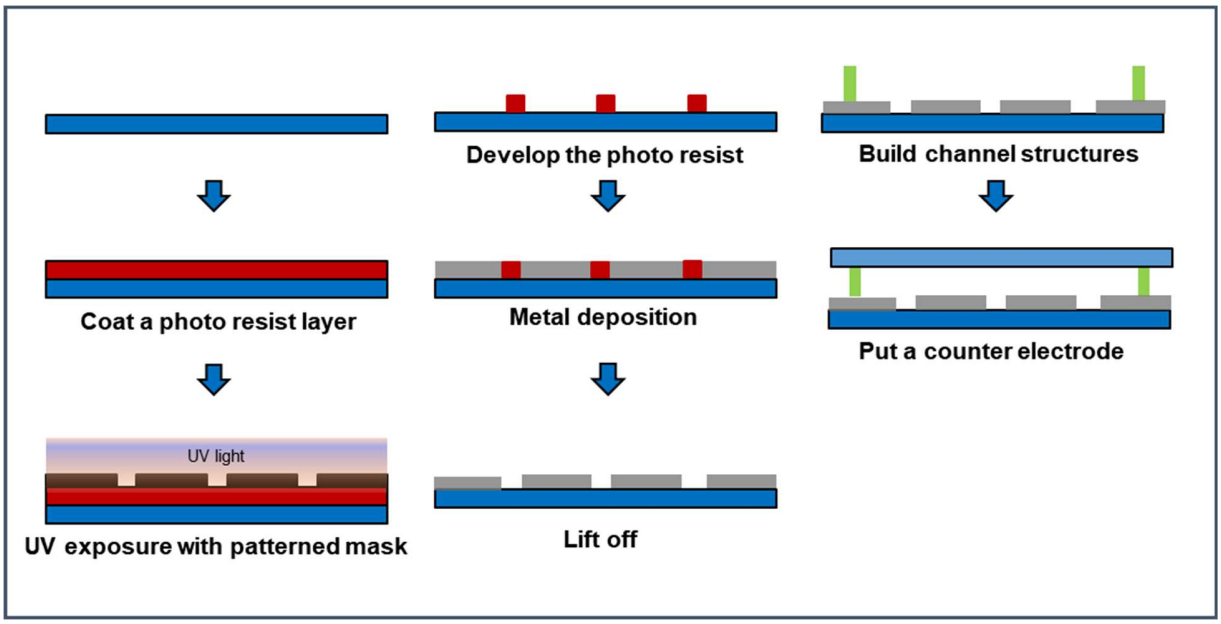

Figure 25. Schematic drawing of photolithography fabrication process used in this study.

3.2.1 Preparation and cleaning

A 3 × 1 inch glass microscope slide substrate was cut into 1 × 1 inch and cleaned through sonication process with ultra-sonication bath for ten-minutes with series of organic solvents, i.e. acetone, methanol, and isopropyl alcohol, in a petri dish, respectively. After the solvent cleaning process, the substrate was rinsed with ultrapure deionized (DI) water (over 18.3 MΩ, Milli-Q system, Millipore, USA) and dried with ultra-high purity nitrogen gas. Thereafter, the glass substrate was immersed in a piranha cleaning mixture solution which is 3:1 ratio of sulfuric acid (NO. 893302, Carolina, USA) and 30 % hydrogen peroxide (868146, Carolina, USA) for 30 mins. After the piranha cleaning process, the substrate was rinsed with ultrapure deionized (DI) water and dried with ultra-high purity nitrogen. After that, the substrate was placed in a convection oven at 65°C for 10 minutes for complete dehydration.

3.2.2 Photolithography

After the cleaning process, surface of the glass substrate is treated by hexamethyldisilazane (HMDS) via chemical vapor deposition (CVD) process. The glass substrate is placed in a vacuum chamber with a container containing HMDS on the bottom. The chamber is vacuumed for 5 minutes through a vacuum pump. After removing the air in the chamber, the vent of chamber is closed for 7 minutes.

The glass substrate coated with HMDS was placed in a spin coater (SCS 6800 Spin Coater, SCS, USA), and 2 ml of photoresist (PR, AZ 5214E-IR Photoresist, Micro Chemicals, USA) was dropped on the surface using a pipette and rotated at 500 revolutions per minute (RPM) for 15 seconds and then 2000 RPM for 30 seconds. Thereafter, the PR coated glass substrate was placed on a hotplate at 100°C for 90 seconds, resulting 1.98 μm thickness of the photoresist.

The PR coated substrate was placed on the UV (ultra violet) mask aligner (PLA-501-FA, Canon, Japan) with a photo mask (soda lime mask, Photo Sciences Inc., USA) which has desired electrode structures designed using computer aided design (CAD) software (Auto CAD 2014, Autodesk, USA). The PR coated substrate was exposed to UV light for 11 seconds at an intensity of 10 mW/cm^2.

The UV exposed substrate was immersed in a developer solution which is a mixture of 4:1 ratio of DI water with developer (AZ 300 MIF Developer, Micro Chemicals, USA) for 50 – 60 seconds. The developed substrate was rinsed with ultrapure DI water and dried by blowing ultra-high purity nitrogen gas for dehydration. Figure 26 represents an array of circular trap pattern for the photolithography process.

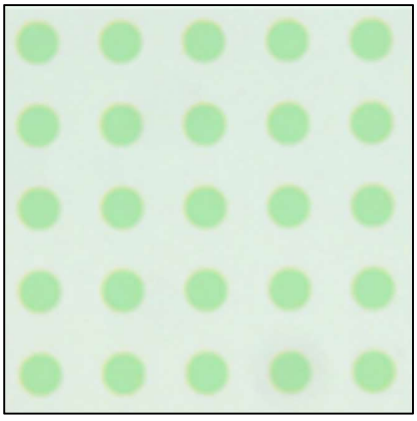

Figure 26. An array of circular trap pattern with the photolithography process.

3.2.3 Metal deposition and lift-off

The substrate on which the trap design pattern is formed through photolithography is subjected to a metal deposition process to have a metal layer to be used as an electrode. This was accomplished through vacuum thermal evaporation process. The substrate was placed at the substrate holder in the thermal evaporator (KV-301-32987-B, Key high vacuum products, USA), and tungsten source basket was filled by pure Chromium (Cr) metal pieces (EVMCR35D, Kurt J. Lesker, USA).

A 1 kÅ of Chromium layer was thermally evaporated from the tungsten basket onto the substrate in a vacuum chamber at a pressure of -4.5 × 10^{-7} torr. The deposition rate was adjusted by controlling the current applied to the basket filament. The applied thermal deposition rate was monitored by a quartz thickness monitor and was measured around 0.3 – 0.7 Å / sec. When the accumulated thermal deposition thickness reaches the desired thickness, the evaporation shutter in the chamber was closed to prevent unnecessary additional deposition and the substrate was allowed to be cooled naturally with room temperature. Figure 27 shows a device in which 1 kÅ of Chromium layer is deposited through the metal deposition process.

Figure 27. A device with 1 kÅ of Chromium layer fabricated by the metal deposition process.

After thermal evaporation, the substrate was inspected for integrity of the thin film metal layer under an optical microscope for cracks and unnecessary impurities. After the integrity inspection, the substrate was immersed in acetone and the unnecessary patterns of photoresist parts was removed with Chromium layer. For effective lift-off, acetone was applied using an air-blower if necessary, or the substrate was sonicated for 1 to 3 minutes with acetone. Then the substrate was rinsed by isopropyl alcohol and ultrapure DI water, and then blow dried with ultra-high purity nitrogen gas. Figure 28 shows the trapping device completed after the lift-off process. The dark area indicates the Cr layer. The small transparent patterns indicate the patterned electrode. Specific patterns out of total 287 different fabricated patterns were used in the DEP trapping experiments.

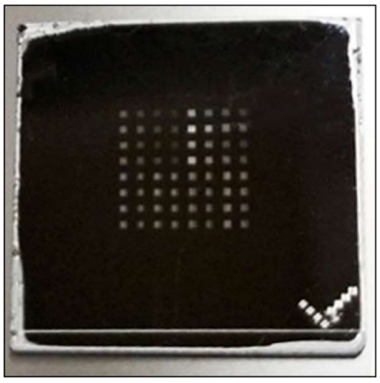

Figure 28. A device after the lift-off process.

3.2.4 Microfluidic flow channel and counter electrode

The microfluidic flow channels were made using the 5, 10, and 30 μm thickness polyethylene terephthalate (PET) spacers (5600, 5601, 5603, Nitto Denko Co, Japan) and the indium-tin-oxide (ITO) coated glass slide (NO. IT10-111-25, NANOCS, USA). The ITO coated glass slide was used as a counter electrode in the trapping device. The double-side sticky PET

spacer enables water-tight bonding between electrode and counter electrode glass slides. The height of the microfluidic channel was determined by the thickness of the PET spacer. In this configuration, the electrode and counter electrode are designed to face each other, different from conventionally used DEP electrode sets. Since the distance between electrode and counter electrode glass slides are limited by the thickness of PET spacer, two glass slides were misaligned 5 mm, so that the electrodes can be connected to the wires. Inlet and outlet holes through the glass substrate were pierced by a highspeed rotary tool with a diamond-coated drilling tip. Through these holes, the liquid media carrying the particles and cells are injected at the inlet using syringe, and removed at the outlet using capillary tubing. Figure 29 shows the completed lab-on-a-chip device after all the fabrication processes.

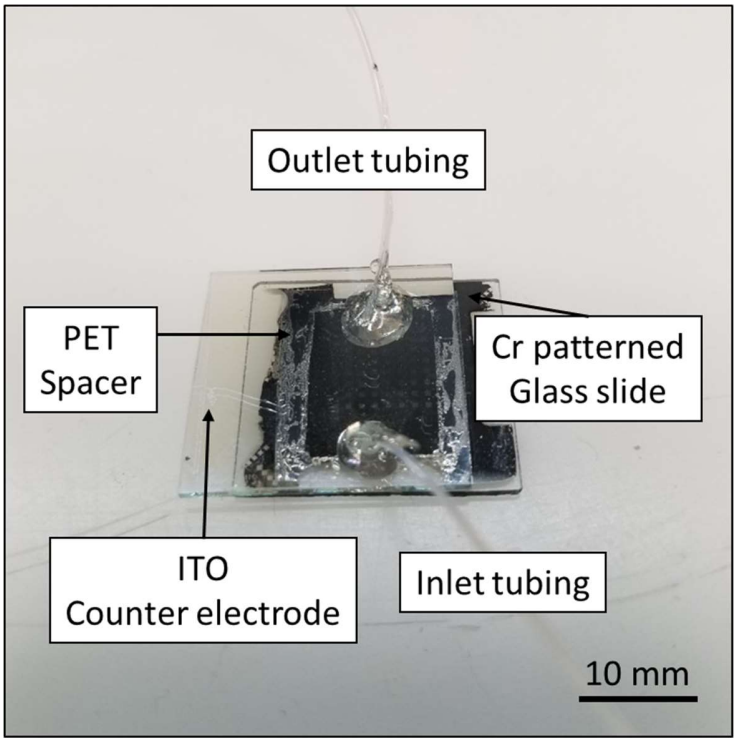

Figure 29. A completed lab-on-a-chip microfluidic trap device.

3.3 Experimental lab-on-a-chip system setup

The dielectrophoretic microfluidic trap system used in this research contains fluidic, electrical, and optical systems. Figure 30 presents Schematic diagram of experimental set-up of dielectrophoretic trap system. Detailed descriptions of each experimental system element are provided separately in this section.

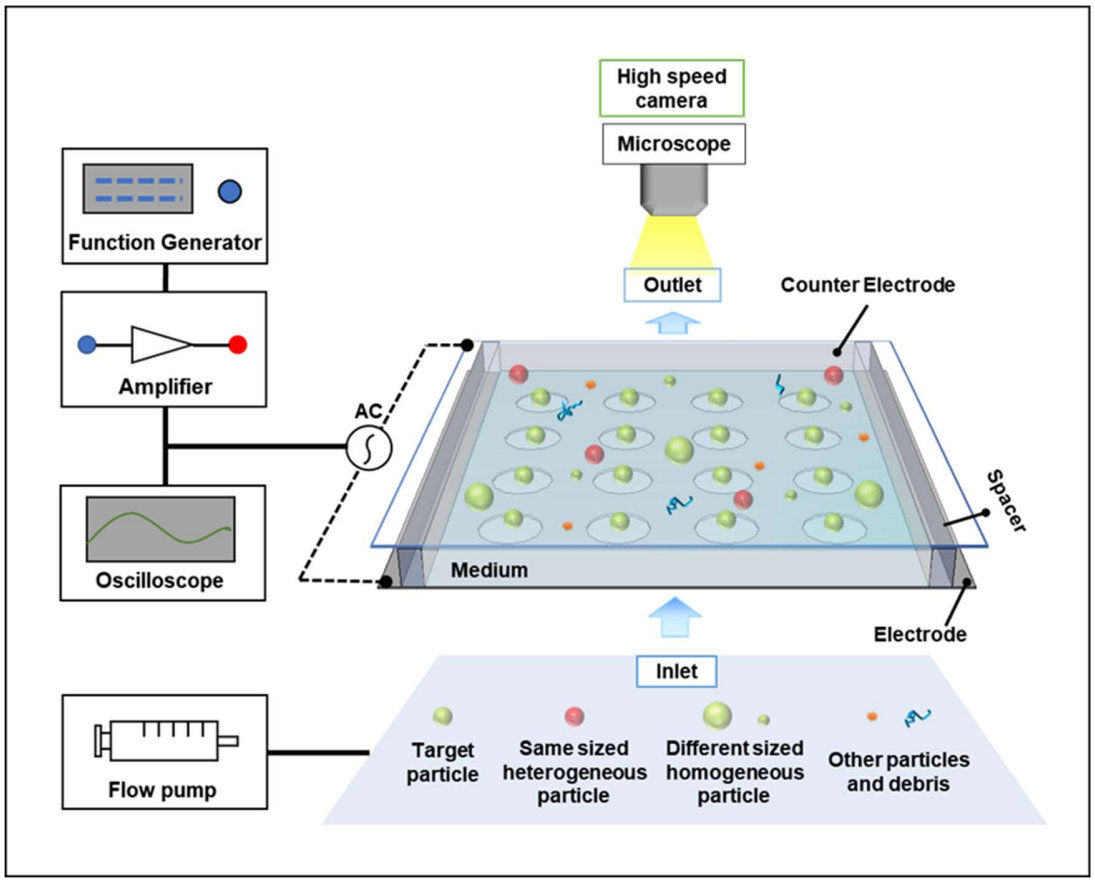

Figure 30. Schematic diagram of experimental set-up of dielectrophoretic trap system.

3.3.1 Fluidic system

The microchannels were connected to inlet and outlet holes pierced in the ITO glass slide. To control steady and accurate flow rate of the fluids with particles, a two-syringe infusion pumps (KDS 200, KD scientific, USA) was used. The inlet channel was connected to a 250 μL syringe (Hamilton Co., USA) that has particle solution and mounted on the syringe pump by a 30 cm long Polytetrafluoroethylene (PTFE) tubing (0.016'' OD, 0.004'' ID, EW-06417-72, Cole-Parmer Co., USA). The outlet channel was connected to the collecting tube with a 10 cm long tubing. The junctions between glass slide and tubing are sealed with epoxy (Quickset, Loctite, Germany) to prevent the leakage.

3.3.2 Electrical system

The DEP electrode and ITO counter electrode were connected to a function / arbitrary waveform generator (33250A, Agilent, Palo Alto, CA) which can supply maximum output of 10 V peak-to-peak from alternating current (AC) of 1 Hz to 20 MHz. When it is necessary to raise the voltage to higher than 10 V, the output signal was connected to a high frequency high-voltage power amplifier (Model 2100HF, TRek, USA) that has 50V/V of fixed gain to boost the output voltage. Also, direct currents (DC) of maximum 72 V, 1.2 A input were supplied by a bench power supply (2200-72-1, Keithley, USA) when necessary. All the magnitudes and duration of the signal were measured using a digital storage oscilloscope (2190D, B+K Precision, USA) in real-time.

3.3.3 Optical system

The trap device was mounted on a microscope (BX53F, Olympus, Japan) with a fluorescent light source (Lumen Dynamics X-Cite Series 120 Q, Excelitas Technologies Co., USA) and a

microscope light power supply (TH4-100, Olympus, Japan). The 4x, 10x, 20x, 50x, and 100x objective lenses were used as necessary. Realtime observation and fluorescence images were taken using a cooled charge-coupled device (CCD) camera (DP-72, Olympus, Japan), and a high-speed camera (Bonito CL-400, Allied Vision Technologies, USA) with a frame grabber (PIXCI-E4G2, EPIX Inc, USA). Up to 384 frames per second was of high-speed images and videos were recorded to analyze movements of single particles with a digital image acquisition software (XCAP™ Standard V3.8, EPIX Inc, USA).

3.3.4 Experimental device setup

To mount the trap device on the conventional microscope station, customized device holder was designed using the SketchUp (V2016, Trimble, US) three-dimensional (3D) design software as shown in Figure 31 and fabricated by a 3D printer (FlashForge Creator Pro, FlashForge Corporation, China). The device holder has 1 inch by 1 inch square groove to accommodate the bottom part of the device, and a bigger square groove for placing the ITO counter electrode. Two wire channels were designed to connect the electrodes with signal sources, and the grooves that can be mounted on the microscope station are also located. The center of the holder is empty so that the inside of the microfluidic channel can be easily observed from top or bottom with an upright or inverted optical microscope, respectively. Figure 32 shows the holder with a trap device and electrical wires connected.

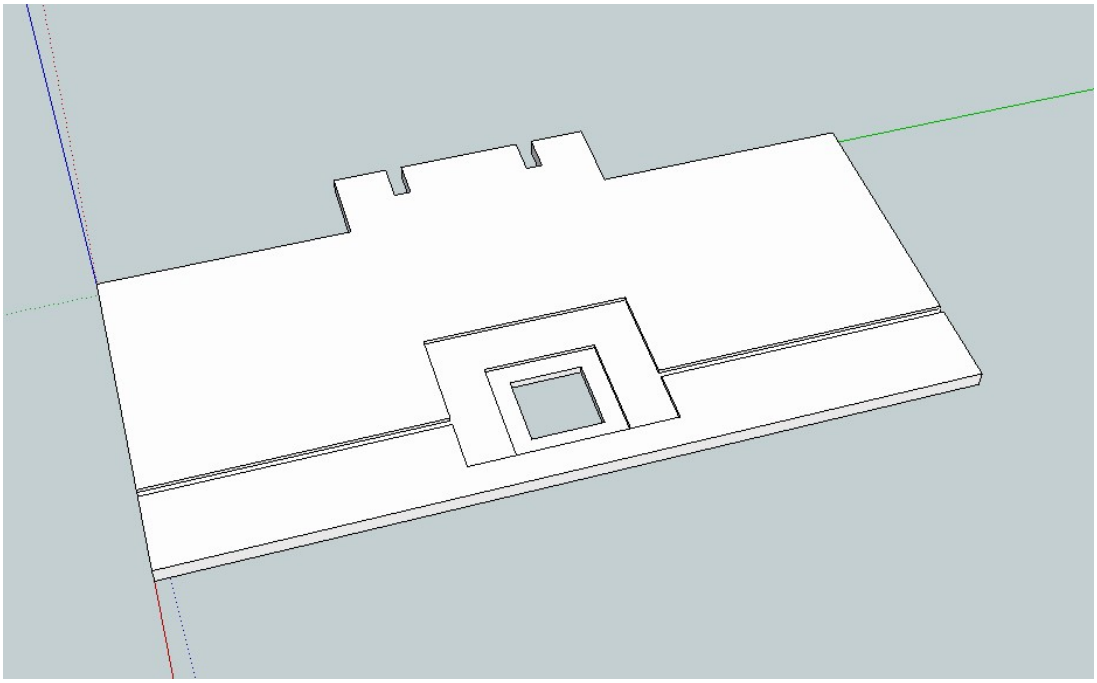

Figure 31. Design of the customized device holder in SketchUp 3D designing software.

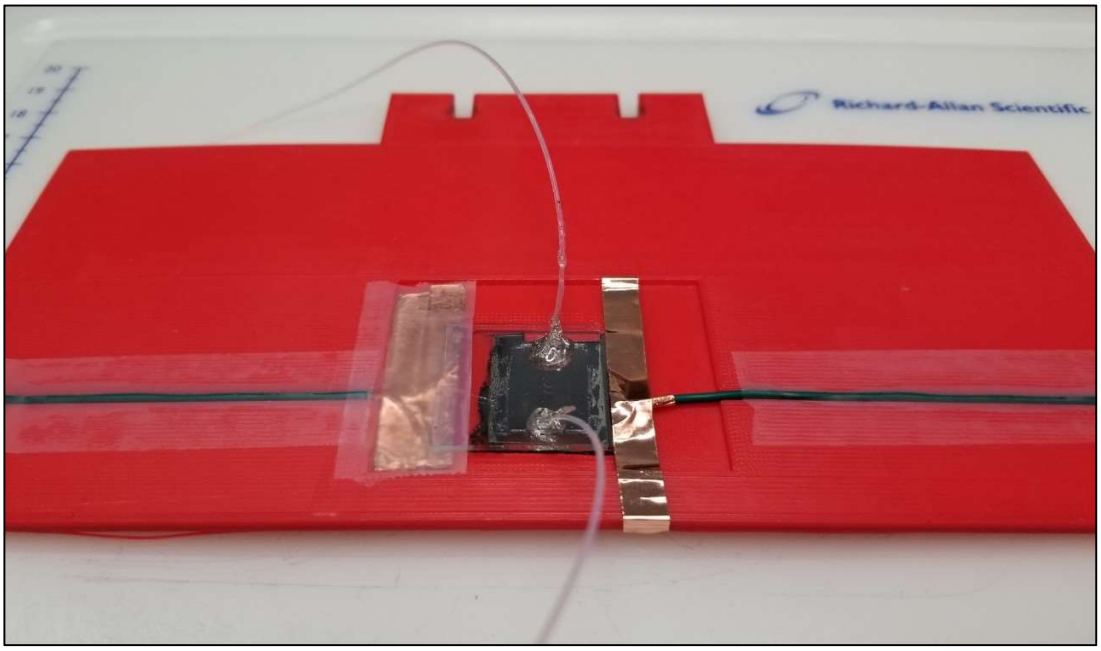

Figure 32. A customized holder with a trap device and electrical wires connected.

Chapter 4

Experimental Methods for Particle Isolation and Immobilization by the Dielectrophoretic Microfluidic Trap System

4.1 Overview

The ability to isolate and pattern individual particles at specific locations based on their physical and chemical properties enables a wide range of biomedical single cell studies, for example disease diagnosis, genetic analysis, drug screening, and tissue engineering [27, 1]. Over the past decade, microfluidic lab-on-a-chip device approaches have been used for single particle isolation and analysis as those allow to manipulate fluidic control of small volumes thus to analyses cellular dynamics and discover regulatory mechanisms [28–32]. In general, larger particles have been considered to be more easily separated because their mass and size are more affected by inertia [33], filtering [34], and electrical forces [35] in microfluidic devices. Also, lower flow rates have been preferred since target particles need a long residence time to be exposed to the force field in DEP [33, 36]. Moreover, lower and narrower channel size have been preferred to easily trap or concentrate particles to a monolayer [29, 31]. Larger attainable electric forces are obtained by decreasing channel height [36–38].

Since the DEP can manipulate particles with high precision force control, designed orientations, and massively parallel processing, the DEP has been exploited in various applications from fundamental researches to practical applications such as dynamic cell trapping and patterning [39–41], cell sorting and isolation [42–44], drug discovery and delivery [41, 45–48], and intermolecular force measurement [18]. Also, the emphasis on bio-particle related DEP research has been steadily increased over the past two decades [49]. However, such previous DEP studies have been stayed with the general strategies of separation related to the size, flow rate and channel height for particle separation and isolation.

In this chapter, I report a strategy that overturning common sense that larger particles, lower flow rates, and smaller, narrower channel sizes will make particle separation easier, and

demonstrate a device for selective single-particle isolation and patterning. I fabricated a simple chromium circular trap microelectrode array on a glass substrate with ITO counter electrode to form an omni-directional DEP force to the center of the circular trap as well as to easily observe behaviors of particles while trapping and patterning. I demonstrate trapping experiments with micro- and nano-sized polystyrene beads as model particles that are currently used in the field of drug delivery due to their ease of surface functionalization, drug loading capacity, and stability in biological media [50–52]. Using the developed trap device, individual particles were selectively trapped on each circular trap in an array by negative DEP (n-DEP) force with various channel height and velocity of particles. The particle trapping efficiency was evaluated according to the height of the microchannel structure, and individual particle trapping behaviors were observed according to the velocity and position of the particles around the trap. In addition, selective trapping experiments for various sizes of micro- and nano-sized particles were performed and compared.

4.2 Micro particle trapping and patterning

Figure 33 shows the schematic illustration of the dielectrophoretic corral trap system in which an AC signal is applied to the electrodes. The DEP forces are generated by an introduced AC signal on the trap electrode and counter electrode located at the bottom and top side of the microfluidic device. Before the AC signal is applied, particles suspended in media are freely traveling by fluid flow introduced by the syringe pump. When the AC signal is applied, the particles around traps are trapped in the circular trap area by negative DEP forces.

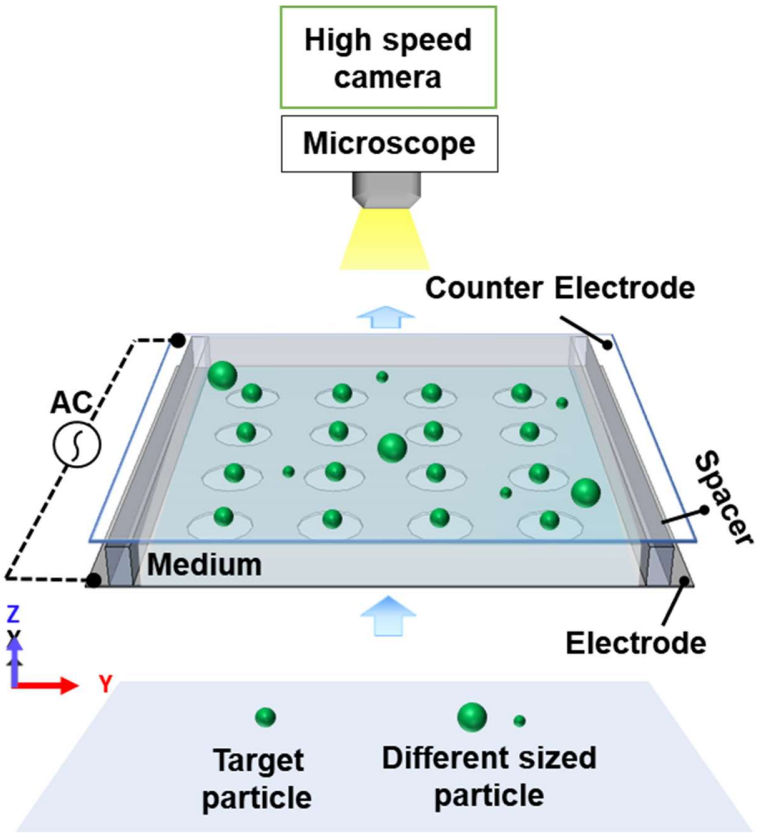

Figure 33. Schematic illustration of the dielectrophoretic corral trap system for particle isolation and patterning.

4.2.1 Numerical analysis to trap 2 μm particles

Firstly, the trapping of 2 μm radius polystyrene particles was observed. Figure 34 represents the numerically simulated direction and magnitudes of the negative DEP force around trap when 1Mhz 8Vp-p was applied on the 40 μm circular trap electrodes to trap a 2 μm radius polystyrene particle. In the figure, the particle was intentionally inserted for better understanding. Each arrow represents the magnitude of the negative DEP force to the particle at the position and illustrates the circular trap provides omnidirectional and symmetrical characteristics of the DEP force to trap particles. As shown in the figure, the particle is pulled toward the center of the circular trap where the electric field gradient is lowest by applying the negative DEP force. Outside the electrode of the trap, the DEP forces are pointing outward, which is a critical element for selective trapping of the particles depending on velocity, physical, or electrical characteristic of the particles.

Figure 35 presents the calculated negative DEP force on a 2 μm radius particle around a trap. For X-axis DEP forces of the graph, negative values indicate the X-axis DEP force acting in the left direction, and positive values indicate the X-axis DEP force acting in the right direction. The X-axis DEP force acts to reduce or increase the movement of particles in the channel, and the balance of the X-axis DEP forces hold particles trapped within the trap in place. The X-axis force has a repulsive force outside the circular trap and converges to the center inside the trap. For Z-axis DEP forces, negative values represent downward Z-axis DEP force that closer to the trap surface, and positive values represent upward Z-axis DEP force. The downward Z-axis DEP force acts together with the gravity, and thus pulling the floating particles in the channel toward the surface of the trap and holding the trapped particles on the bottom of the trap. In the graph, the Z-axis force is directed vertically upwards from the surface around the rim, and downwards from inside the trap. As particles moving in the direction of X-axis travel into the trap, they are centered

by symmetrical Y-axis forces on both sides, so the Y-axis force at the center is negligible compared to the X- and Z-axis forces.

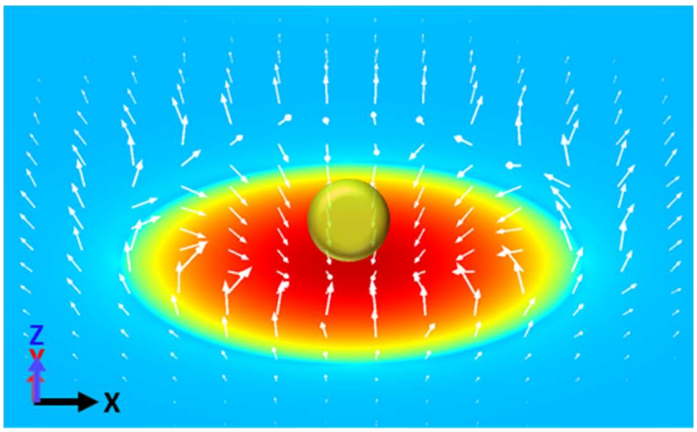

Figure 34. Simulated electric field and DEP force direction on a 2 μm radius polystyrene particle around a trap. For negative DEP forces, the bead is aligned at the center of the electrode by the omnidirectional DEP forces.

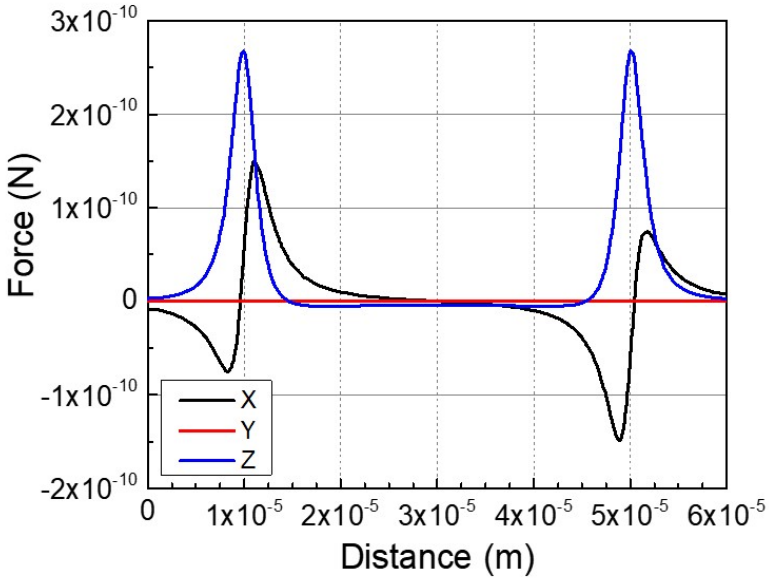

Figure 35. Calculated negative DEP force on a 2 μm radius particle around a trap.

4.2.2 Trapping 2 μm polystyrene particles

Figure 36 and Figure 37 show the results of trapping experiment using 2 μm radius polystyrene particles. The particles in the medium are flowing through the microchannels with no applied voltage on the trap electrodes. When the AC 1 MHz 8 $V_{peak\text{-}to\text{-}peak}$ of electrical signal was applied on the electrodes with 40 μm traps and 40 μm gaps, the 2 μm particles were captured and immobilized in each circular trap by the negative DEP force as shown in Figure 37. Since there is flow pushing the particles from the inlet to the outlet direction, the trapped particles are held slightly offset from the center in the direction of balancing the fluid flow and the DEP force.

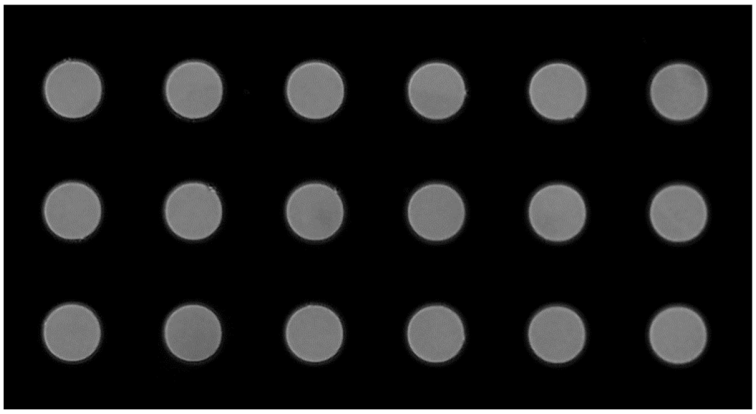

Figure 36. No electrical signal was applied on the traps.

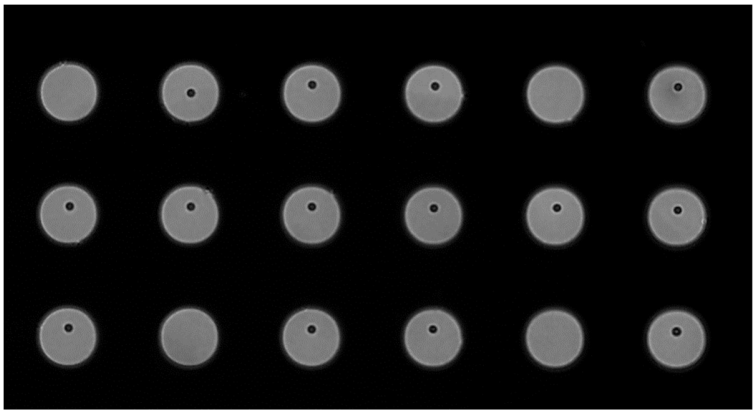

Figure 37. 2 μm polystyrene particles were trapped in each trap.

4.3 Trapping efficiencies with various channel heights and velocities

I explored the efficiencies of the DEP trap as the channel height was varied. I have investigated the optimal channel structure for trapping by changing the height of microchannel of the trap devices. The height of the trap device microchannels varied with the height of the PET spacers (5600, 5601, 5603, Nitto Denko Co, Japan) used in the microchannel fabrication process. I fabricated devices with 5, 10, 20, 30, and 40 μm heights, respectively, and performed 2 μm radius polystyrene microparticle trapping experiments.

Figure 38 shows trapping efficacies for particles traveling through seven 40 μm circular trap arrays in series at 5, 10, 20, 30, and 40 μm height channels when 1 Mhz $8V_{peak\text{-}to\text{-}peak}$ was applied on the trap electrodes. Particles that were free to move along various fluid flows within the channel of each height device were trapped by the n-DEP force. The velocities of the trapped particles and untrapped particles were recorded as binomial. The binomial outcomes of trapping efficiencies were fitted using R package 'mgcv' [53, 54]. As shown in Figure 38, each 5, 10, 20, 30, and 40 μm height channels had a maximum efficiency of 0.177 at 207 μm/s, 0.285 at 223 μm/s, 0.489 at 290 μm/s, 0.783 at 466 μm/s, and 0.407 at 286 μm/s respectively.

Figure 39 shows the counts of trapped particles and total efficiencies at each channel height. The total efficiencies were evaluated from the ratio of trapped particles to untrapped particles in each trap device, regardless of the velocity of the particles. For each 5, 10, 20, 30, and 40 μm height channels, 174, 208, 230, 234 and 230 of 2 μm polystyrene particles were analyzed and the efficiency of each channel was 13.22, 12.5, 23.48, 55.56, and 25.22% respectively.

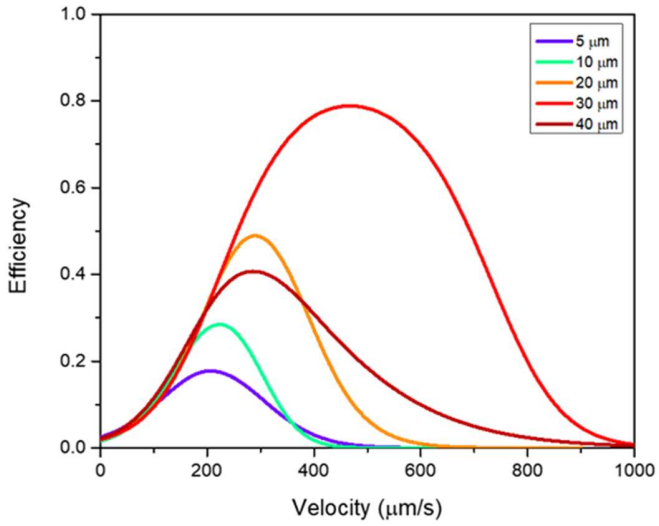

Figure 38. Trapping efficiencies of 5, 10, 20, 30, and 40 μm height channels for 2 μm radius particles with various velocities.

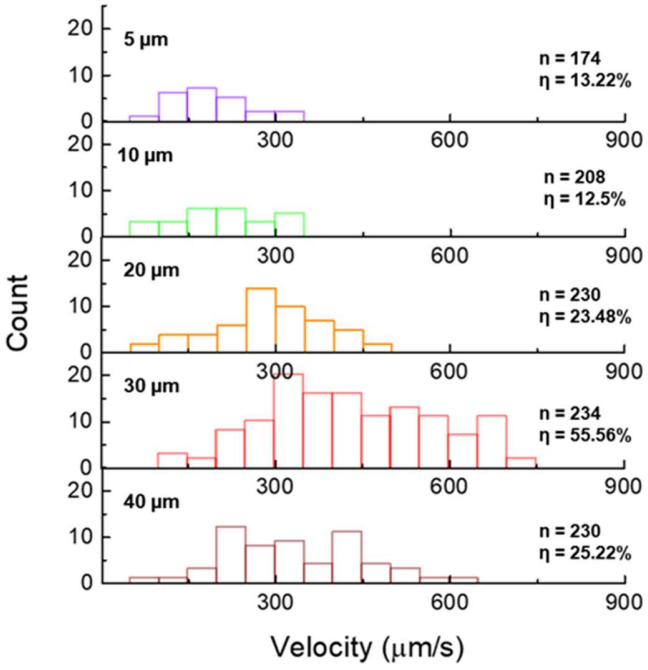

Figure 39. Histogram graph presents the number of the trapped 2 μm radius particles with 5, 10, 20, 30, and 40 μm height channels.

4.3.1 Comparison of the DEP forces according to the channel heights

In order to compare the trapping efficiency at each channel height with the magnitude of the X-axis and Z-axis DEP forces, a numerical simulation was performed. Figure 40 shows the X-axis DEP forces exerted on 2 μm polystyrene particles at the surface of each height channel. The strongest X-axis forces toward inside at the edge of the electrode at each 5, 10, 20, 30, and 40 μm height channel traps were 0.76, 0.59, 0.3, 0.18, and 0.12 nN, respectively. The DEP forces of the X-axis for particle trapping were analyzed to be stronger at lower channel heights.

Figure 41 shows the Z-axis DEP forces exerted on 2 μm polystyrene particles at the center of the surface of each height channel. The strongest Z-axis forces pulling particles toward the bottom of the trap center at each 5, 10, 20, 30, and 40 μm height channel traps were 62.5, 35, 17.25, 10.5, and 7 pN, respectively. As same as the DEP forces of the X-axis, the DEP forces of the Z-axis for particle trapping were analyzed to be stronger at lower channel heights.

According to this simulation, DEP forces at all positions for trapping particles were analyzed to be stronger as the channel height was lowered. This is because the electric field formed in the channel becomes stronger as the distance between the chromium electrode and the ITO counter electrode becomes closer. However, the trapping efficiencies at each channel height in the previous section were not agreed with the increasing strength of the X- and Z-axis DEP forces as the height was lowered. Therefore, it is necessary to analyze the particle behavior when the particles are trapped or untrapped in the trap of the channel.

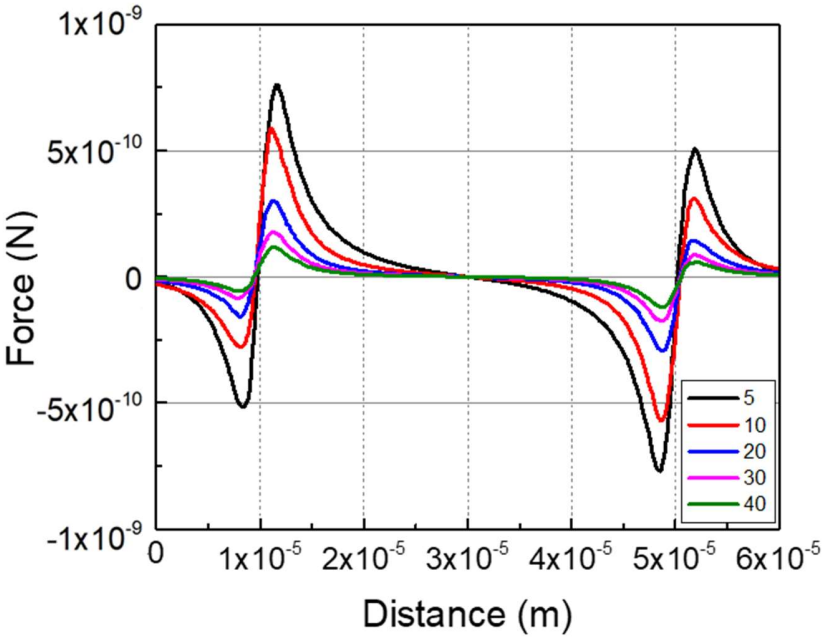

Figure 40. Comparison of the X-axis DEP forces according to the channel heights.

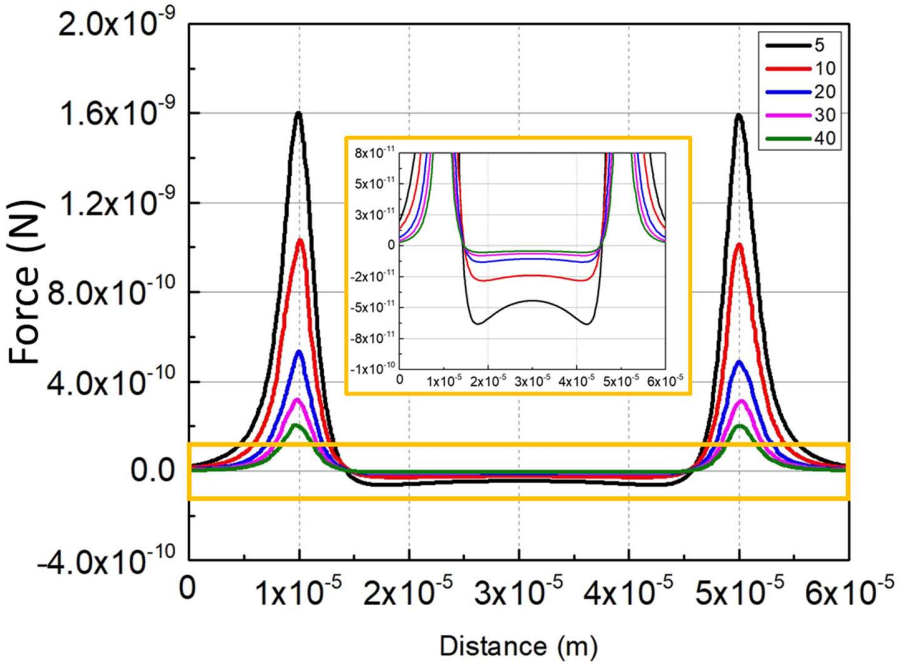

Figure 41. Comparison of the Z-axis DEP forces according to the channel heights.

4.4 Particle height identification

Since an optical microscope can only acquire two-dimensional images of particle movements, in order to analyze the behavior of three-dimensional particle movements, a method was needed to identify the height of the particles obtained from the experimental images.

4.4.1 Image-matching method

The image-matching method was used to determine the height of the particles in the medium of the trap device [55, 56]. The main concept of the image matching method is to match the standard images of a particle of known height with the images of a sinking particle. First, a 2 μm radius particle on the surface of the device were focused by the microscope. Then, images of the particle with increasing height by 500 nm by the microscope stage were recorded. To record images of the sinking particle, a particle solution was dropped on the electrode surface of the device and the counter electrode was fixed, and the images were immediately recorded. The images of the sinking particles were recorded at 5 frames per second using the high-speed camera. The two recorded images were matched to obtain the particle height of each image frame of the settled particles as shown in Figure 42.

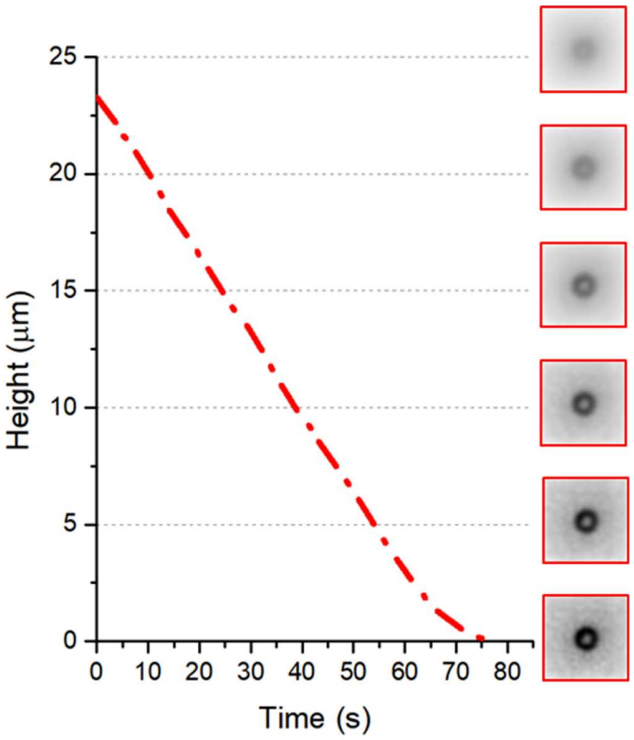

Figure 42. Particle height determination by image-matching method.

4.4.2 Generation of defocused microbead images

Microbead images at different heights above the bottom electrode were generated using the theoretical point spread function (PSF) for the optical imaging setup. The microscope objective is an air objective (LMPlanFL N 20x; Olympus) with a numerical aperture of 0.40 and a working distance of 12 mm, designed for use without a coverslip. In order to account for the insertion of a ITO coverslip between sample and microscope objective in the experiments, the theoretical PSF was calculated using rigorous vectorial theory that allows for up to three stratified media (immersion medium, coverslip, and sample medium) and properly accounts for mismatches in coverslip thickness as well as refractive indices relative to the design values parameters [57] (PSFLab version 3.5, OneMolecule; psflab.app). The point spread function of the experimental setup was approximated by the illumination point spread function, assuming uniform illumination with plane polarized light at a wavelength of 550 nm. The following actual refractive indices were used for the calculation: 1 for the immersion medium (air), 1.52 for the coverslip (BK-7 glass covered with a thin ITO layer, assumed to have negligible contribution to the refractive index), and 1.33 for the sample (approximated as pure water); the actual value of the coverslip thickness was set to the experimental value of 1.1 μm. A design value of 1 was used for the refractive indices of both immersion medium and coverslip, which effectively disables the coverslip layer in the design case (the design value for coverslip thickness is then without influence and arbitrarily set to 1 nm).

In the experiments, the microscope objective was focused onto the bottom electrode. This focusing step was simulated in a 1D PSF calculation along the optical axis using PSFLab's scan mode, which allows to determine the proper placement of the sample relative to the microscope objective. In scan mode, the objective is moved relative to the sample, and the intensity of a

(hypothetical) on-axis point probe located at a fixed depth from the sample-coverslip interface is displayed as a function of that movement (specified by the coverslip position). The point probe depth was set to the height of the channel (30 μm), which puts it on the surface of the bottom electrode. The point of highest intensity - which we will define as the focus - was obtained for a coverslip position of a = - 365.35 μm. The "a" and "z" axis are antiparallel and share the origin.

This value was subsequently used for generating a real-space map of the 3D PSF. For the final image convolution step, the XY coordinates were set to use the same pixel spacing as the experimental images (0.35 μm / pixel), and covered a range from - 10.5 to + 10.5 μm (31 points) in both X and Y directions. The Z range extended from 365.35 μm (sample-coverslip interface) to 395.35 μm (bottom electrode) in steps of 508.5 nm; all other computational parameters were the same as before.

The original, undistorted bead image was obtained from the deconvolution of an experimental in-focus bead image with the 2D PSF of the focal plane (bottom electrode). For this purpose, the in-focus bead image (taken with a color camera) was converted to an intensity image by summing the values of the red-green-blue (RGB) color channels, and the resulting grayscale image was intensity-inverted, centered, and cropped to 50 × 50 pixels. The deconvolution was carried out using the Richardson-Lucy algorithm [58, 59] with a regularization constraint based on total variation [60] as implemented in DeconvolutionLab2 [61], using a low level of regularization, a cap of 150 iterations, and a non-negativity constraint. The resulting image was then convolved with the individual Z slices from the calculated 3D PSF to obtain the defocused bead images at the different heights within the channel. In order to reduce convolution artifacts due to the square geometry, the PSF Z slices were circularized by setting values in the corner areas to zero.

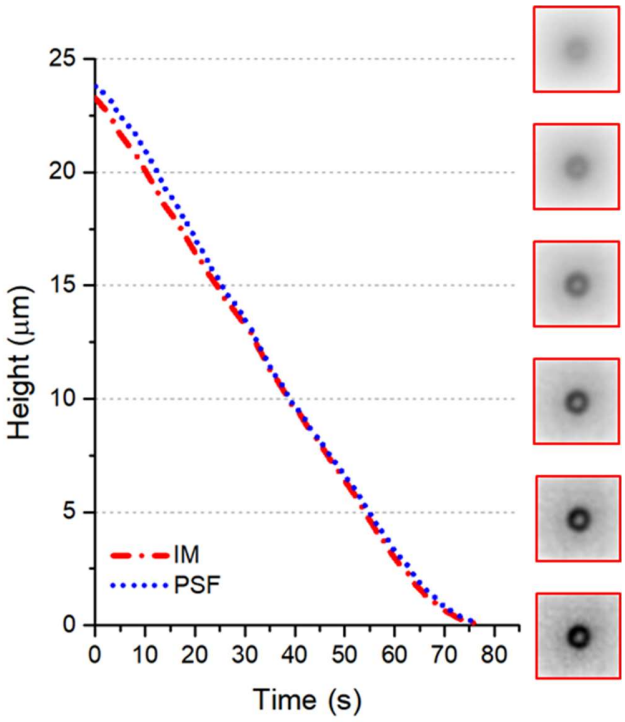

Figure 43. Comparison of IM and PSF height determine methods

4.4.3 Numerical simulation of particle sedimentation

The sedimentation of the particles settling to the bottom of the microfluidic device is the interaction of gravity and buoyancy [55, 62] as

$$F_{Sedimentation} = F_{Gravity} + F_{Buoyancy} = \frac{4}{3}\pi r^3(\rho_{Particle} - \rho_{Medium})g \quad (8)$$

where r is the radius of the particles, $\rho_{Particle}$ is the density of the particles, ρ_{Medium} is the density of the medium, and g is the gravity constant. During particle sedimentation, the initial height equation of a mass m can be described as

$$m\frac{du}{dt} = F_{Sedimentation} + F_{Viscosity} \quad (9)$$

where m is the mass, u is the sedimentation velocity. According to the Stokes' law, the viscosity of the sphere can be expressed as [63]

$$F_{Viscosity} = 6\pi r\eta uK \quad (10)$$

where the η is the dynamic viscosity of the medium and K is the correction factor of Stokes' law when a sphere particle is approaching a long plane surface in perpendicular. The correction factor K is

$$K = \alpha\frac{r}{h} \quad (11)$$

where α is a constant determined by the size and density of the particle, h is the gap between the surface of the plain and the particle.

The equation of this Stokes' law was numerically analyzed by COMSOL Multiphysics (V5.3. COMSOL Inc, Sweden) with particle tracing module include wall corrections. The fluid flow in the channel was assumed to be stationary, and the time-dependent location of the 2 μm radius particle from the 25 μm height to the surface was analyzed using the time-dependent solver. Figure 44 shows the time-dependent sedimentation position of the particle calculated by the

numerical analysis. The results of the numerical analysis are comparable to the two methods described above.

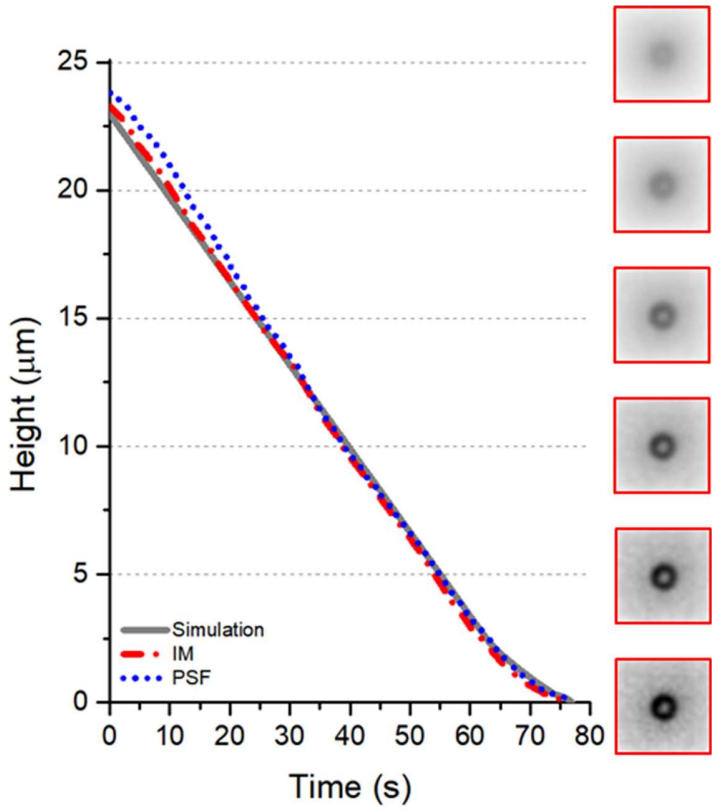

Figure 44. Numerically calculated time-dependent sedimentation of a 2 μm radius particle.

4.5 Trapping behavior around the trap

I analyzed the behaviors of the particle movements around the trap in 30 μm channel height which has the highest trapping efficiency. To analyze the behavior of the particles around the trap, I first classified the trapped particles and the untrapped particles. Figure 45 presents a scatter plot of trapped and untrapped 2 μm radius particles with heights and velocities in 30 μm height channel. Trapped particles are marked with an O symbol, and untrapped particles are marked with an X symbol. Each of six independent experiments showed reproducibility for the pattern of trapping and it is observed that particles are trapped with specific ranges of height and velocity within the channel. For example, particles with a velocity of less than 300 μm / s and a height of less than 5 μm were not trapped, and particles faster than 700 μm / s were not captured at any height. Velocities between 200 μm / s and 650 μm / s had both trapped and untrapped particles, and untrapped particles were located at higher height locations than trapped particles. The height of the trapped particles decreased as the velocity of the particles increased. Also, as the velocity increased, the lowest height of the untrapped particles was also lowered.

The behavior of the trapped particles and the untrapped particles around the trap can be explained by the following cases as shown in Figure 46. The trapped particles have two cases of behaviors. When particles are moving in an appropriate velocity and enough height to be pulled down by the Z-axis of the DEP force and to avoid the repulsive force of the Y-axis, it would be pulled down and trapped as Figure 46 A. When particles are moving in an appropriate velocity and lower height (not on the surface), it would be lifted by the Z-axis repulsive force avoiding the X- and Y-axis repulsive force around the edge and trapped by the Z-axis pulling force as Figure 46 B. In addition to the cases of trapped, the untrapped particles also have two cases of behaviors. When particles move too fast to be trapped, the particles are untrapped because the trapping force could

not overcome the kinetic energy of the particles, or when particles are moving at a too high location from the trap, it would be untrapped because the Z-axis pulling force decreases as the height of the particles as shown in Figure 46 C. When particles are moving in a slow velocity, the particles are sunk toward the surface by the gravity. Since the low velocity, it would be hard to overcome the repulsive Y-axis DEP force at the edge of the trap, it can be pushed by the repulsive force near the edge of the trap, therefore, the particles are bypass the trap as shown in Figure 46 D. In the next section, the behavior of the particles was experimentally analyzed and discussed.

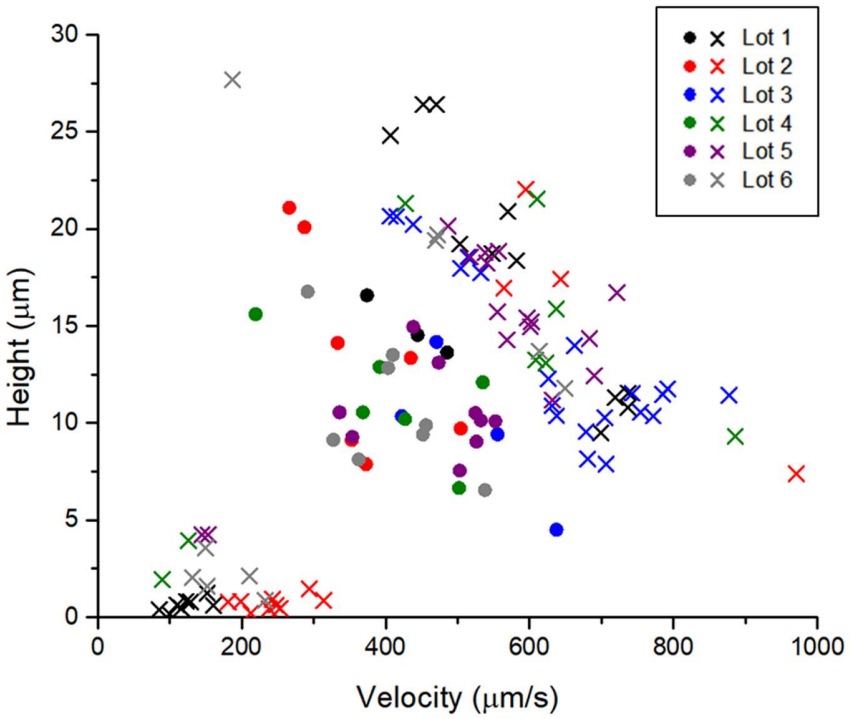

Figure 45. Scatter plot of trapped and untrapped 2 μm radius particles.

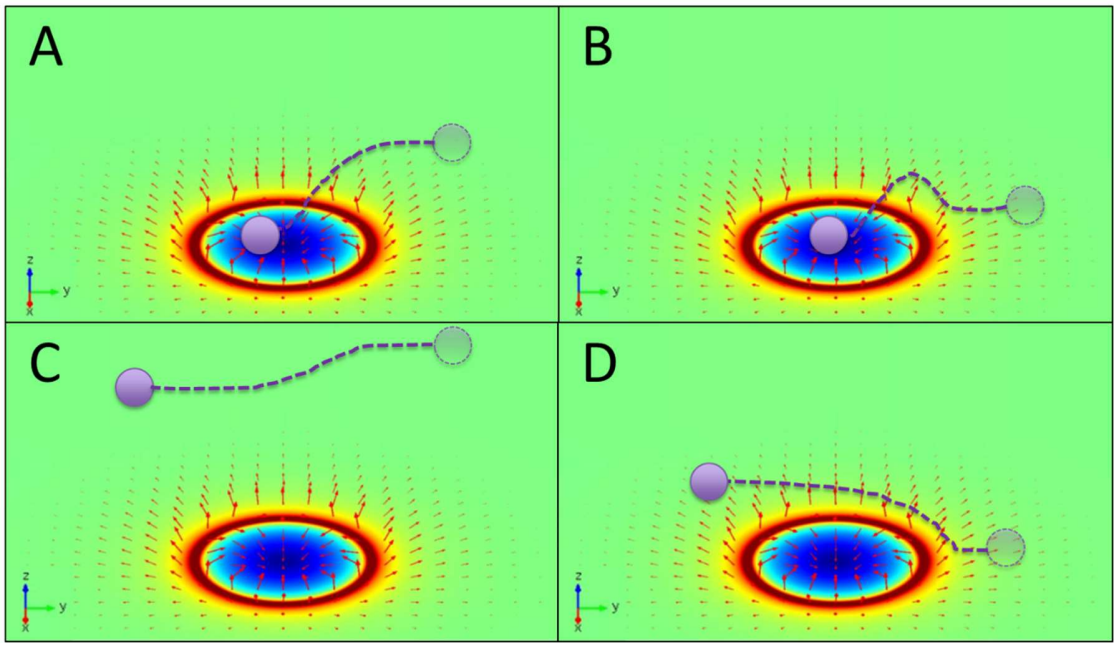

Figure 46. Behavior of particles around trapped. (A, B) Trapped particles, (C, D) Untrapped Particles.

4.5.1 Particles near surface

Figure 47 presents behaviors of particles moving at low velocities which are gravitationally sunk toward the surface. Since the low velocity, the particles having difficulties overcoming the X-axis repulsive force. Also, since it is difficult to approach the exact center of the outer arch of the trap which has the symmetric Y-axis force, the repulsive force eventually forces the particles to bypass the trap. Particles approaching away from the center of the X axis of the trap will be bypassed faster than the particles approach the X axis center of the trap. Also, since the Z-axis repulsive forces outside the trap are directed upward, some particles could be lifted from the surface while bypassing the trap.

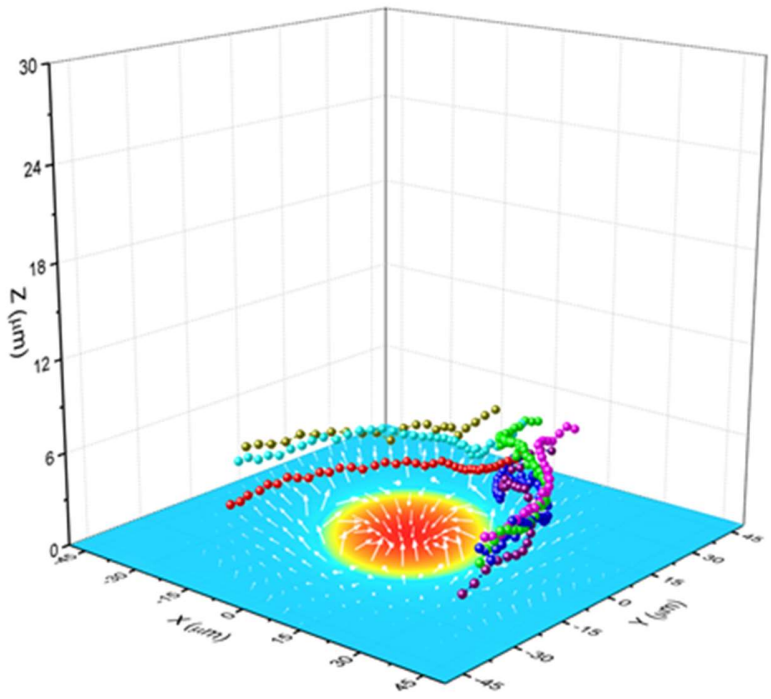

Figure 47. Trajectories of particles near the surface.

4.5.2 Trapped and untrapped particles

Figure 48 and Figure 49 show the behavior of the trapped and untrapped particles. When particles pass over the trap, the Z-axis force pushes the particles upward at near the edge and pulls the particles down at inside of the trap. Since the upward repulsive force decreases with the Z-height position of the particle as shown in Figure 50, the downward pulling force in the trap acts together with gravity to pull the particle towards the bottom of the trap when the particles are at an appropriate height.

The particles in the lower initial position in Figure 48 were relatively faster compared to the particles in the higher initial position but were trapped because they received stronger pulling forces downward. In addition, the particles in the higher initial position are affected by the relatively lower pulling forces; however, the particles move at the lower velocity were trapped since the particles were affected longer by the trapping force.

Figure 49 shows the behavior of untrapped particles, which are either faster at the same height or higher location at the same velocity than trapped particles in Figure 48 except for the particle near the surface.

The comparison of a trapped particle and two untrapped particles at similar heights is shown in Figure 51. The velocity of the black particle was 596.48 μm/s with the initial height of 15.57 μm. It was faster than red particle which has the velocity of 425.43 μm/s with the initial height of 14.96 μm. In addition, the initial height of the blue particle was 13.69 μm which is lower than the height of the red particle, however, the velocity of the blue particle was 648.37 μm/s, which is faster than the red particle, therefore was not trapped.

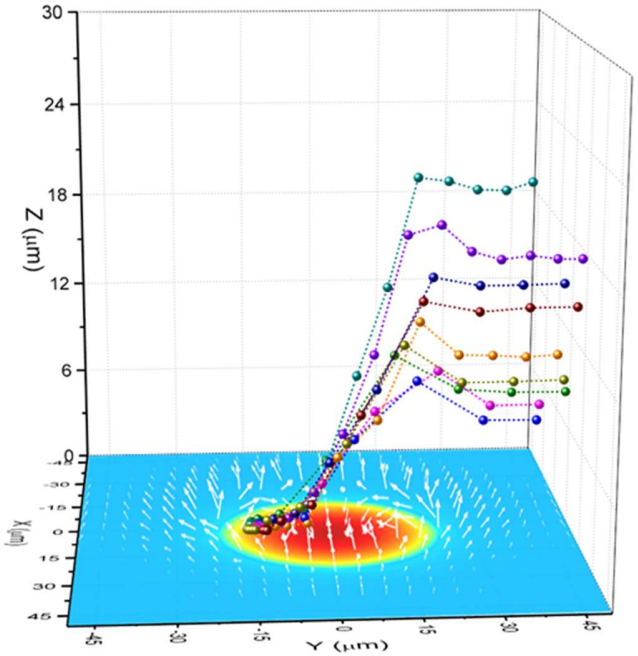

Figure 48. Trajectories of trapped particles.

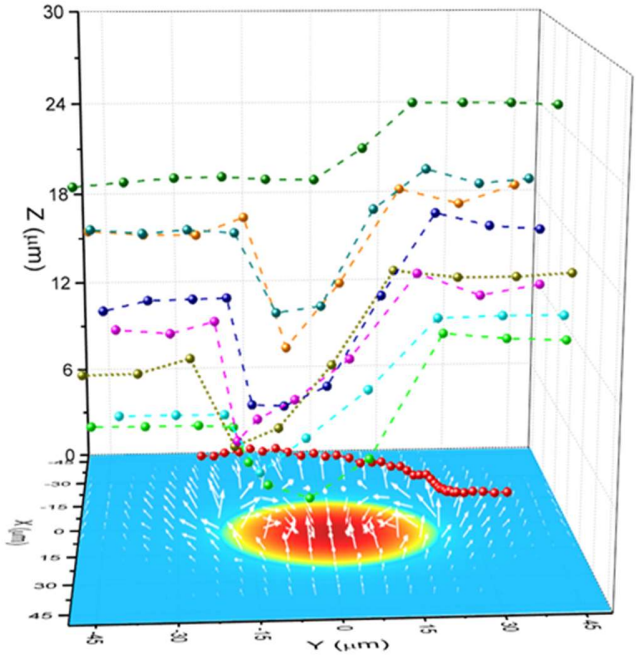

Figure 49. Trajectories of untrapped particles.

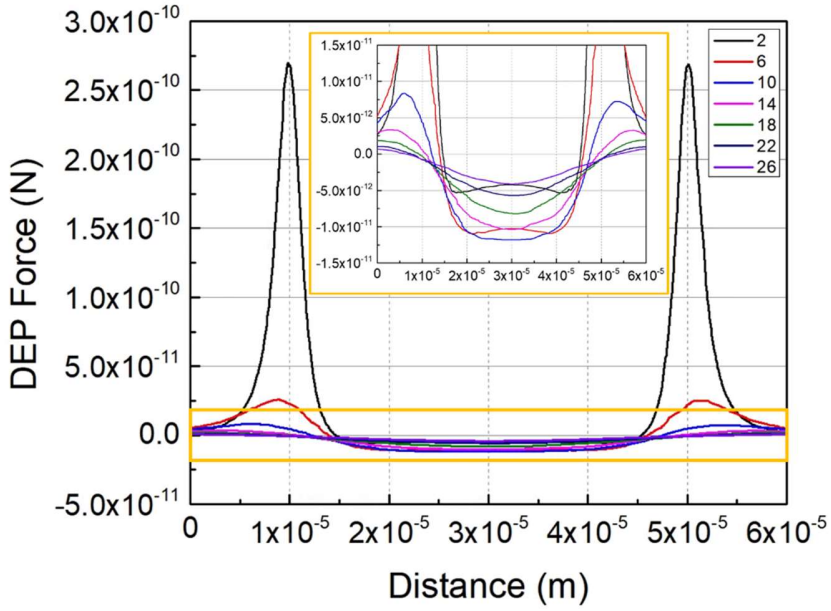

Figure 50. Z-axis forces according to the height position.

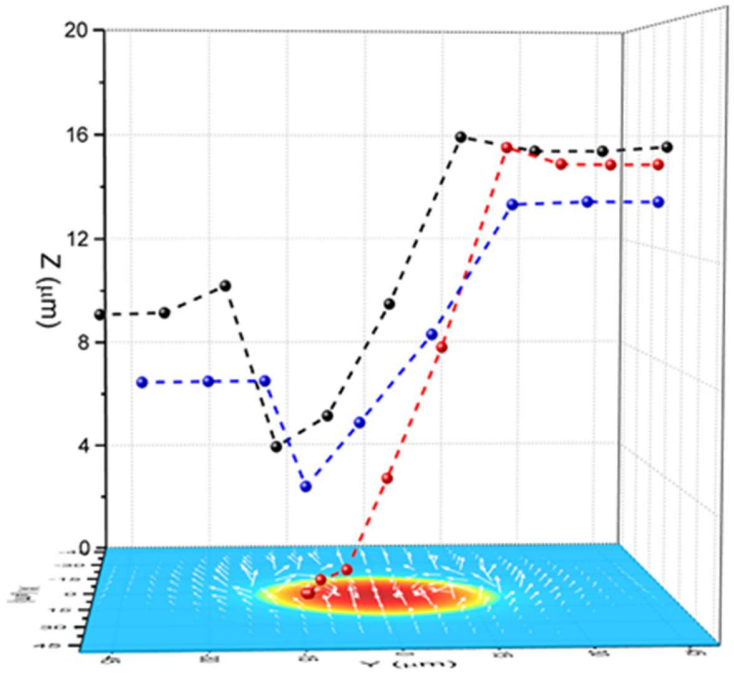

Figure 51. Comparison of trapped (red) and untrapped (black, blue) particles.

4.6 Various size of particles trapping

4.6.1 Work calculation

To quantify and analyze the correlation between the velocity of particles and the trapping force of the trap, the amount of total work stopping the particle was calculated. Since the particle is stopped in the trap not only by the trapping DEP force at the final position but also continuously influenced by the trapping DEP force from the moment it enters the trap until it stops, therefore, the total work was calculated with distance.

Figure 52 illustrates an example of calculating work when capturing a particle in a 40 μm DEP trap. The particle in the figure was moving from left to right along the fluid flow and stopped at 2.5 μm away from the edge of the trap by the DEP trapping force. Here, the work for capturing the particle was calculated by integrating the DEP force at the position where the particles stopped from the center of the trap, that is, a distance of 17.5 μm from the center of the trap.

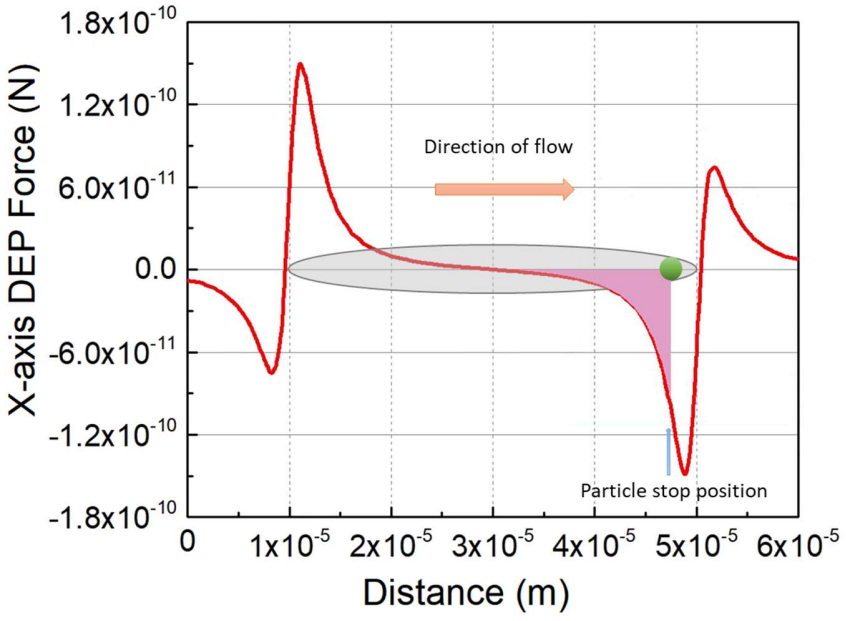

Figure 52. Schematic illustration of work calculation.

4.6.2 Properties of polystyrene particles

In order to calculate trapping forces of particles using the DEP trap, quantitative information of physical and electrical properties of particles are needed. Figure 53 shows the real part of Clausius-Mossotti factors for the particles used in the trapping experiment, calculated for frequencies ranging from 1 kHz to 10 MHz. The Clausius-Mossotti factors were plotted for each frequency after experimentally finding the crossover-frequency of each particle. Particle sizes used in the experiments were 200 nm, 500 nm, 1000 nm, 2 μm, 3 μm, and 5 μm radii and experiments and calculations were performed on DI water with a conductivity of 2 μS / cm.

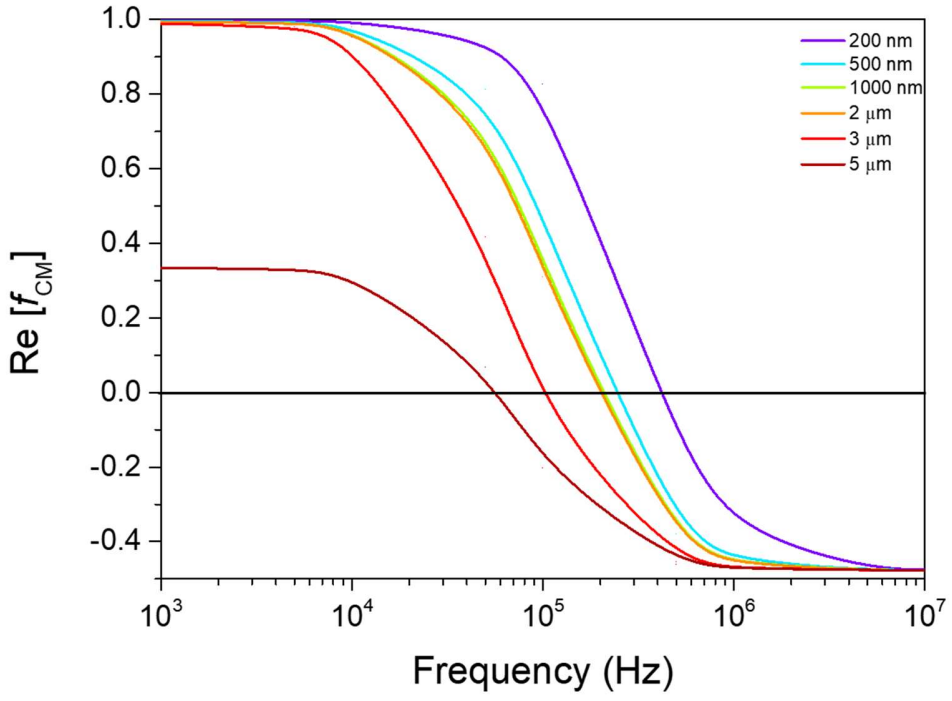

Figure 53. The real part of Clausius-Mossotti factors of particles with frequencies.

4.6.3 Calculation of DEP forces in various sizes of particles

The numerical analysis of DEP forces for each 200 nm, 500 nm, 1000 nm, 2 μm, 3 μm, and 5 μm radii particle in the DEP trap were also conducted to quantify the work required to trap particles under the applied electric fields. Based on the real part of Clausius-Mossotti factors calculated in the previous section, the n-DEP forces in the X-axis where each size particle is affected at each position of the circular DEP trap were calculated through the FEA numerical simulation as shown in Figure 54. The voltage applied to the trap electrodes was fixed as 1 MHz 8 $V_{peak\text{-}to\text{-}peak}$.

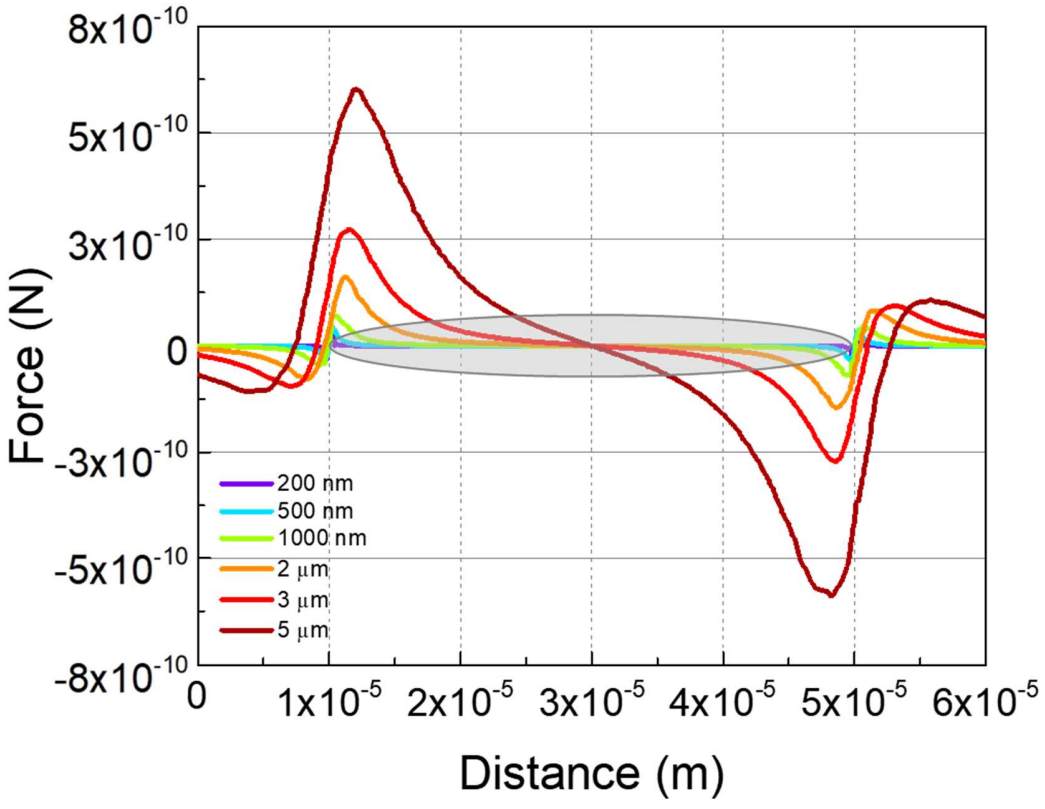

Figure 54. X-axis DEP forces in various sizes of particles.

4.6.4 Trapping various sizes of particles

In order to further investigate the trapping capability of the DEP trap system, trapping experiments of various sizes of particles were performed under the same conditions. In this experiment, 200 nm, 500 nm, 1000 nm, 2 μm, 3 μm, and 5 μm radii particles were used.

Figure 55 presents the velocities of particles and required work to trap the particles. Herein, bigger particles were captured with higher velocities. Each 200 nm, 500 nm, 1000 nm, 2 μm, 3 μm, and 5 μm particles were trapped with the fastest velocity of 13.14, 65.79, 147.37, 442.1, 814.03, and 1494.71 μm / s, respectively. In a similar trend, trapping bigger particles needed more work to be captured due to their high velocity. In terms of the work needed, for the 200 nm, 500 nm, 1000 nm, 2 μm, 3 μm, and 5 μm particles, 1.16×10^{-19}, 3.56×10^{-18}, 2.22×10^{-17}, 1.69×10^{-16}, 5.28×10^{-16}, and 2.16×10^{-15} N · m was required to trap the fastest particle, respectively. The regression of the data is in great agreement with a linear model in 0.9937 of R-Square value. It can be explained that DEP trapping force needed in the DEP trap system is closely related to the radius of the particles when other variables are controlled. In addition, none of the velocity regions overlap, suggesting the possibility of using velocity differentials to separate different sized particles within the DEP trap system.

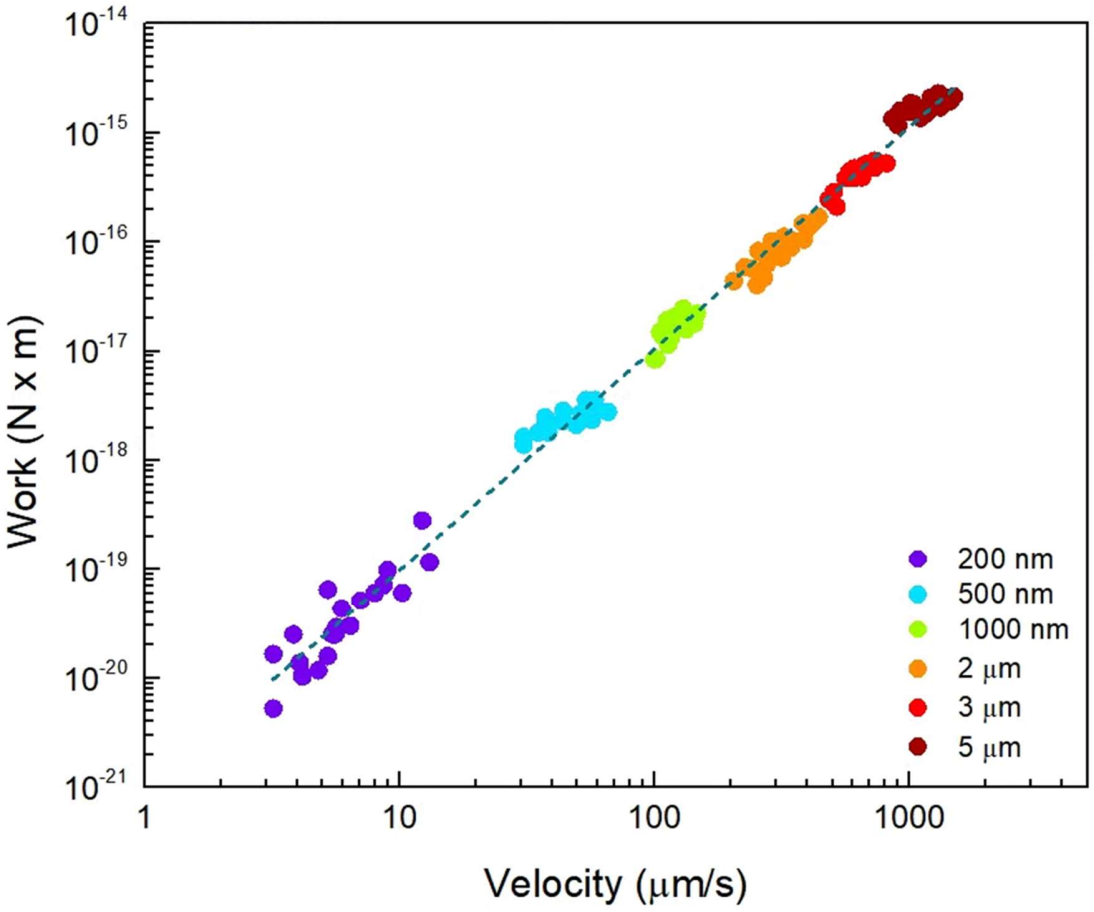

Figure 55. Trapping various sizes of particles.

4.6.5 Verification of single nanoparticles

Because it is difficult to observe small nanoparticles using conventional optical microscopes, the 200 nm nanoparticles used in the previous section were used fluorescent-dyed particles (CFP-0558-2, Spherotech, USA) and were observed under a fluorescence microscope in the experiment as shown in Figure 56. The yellow arrows were inserted to indicate trapped particles. However, since it is difficult to determine that the particle observed with fluorescence was a single particle, the singleness of the 200 nm particles was evaluated. Firstly, the 200 nm nanoparticles were trapped by positive DEP (1 kHz, 10 $V_{peak\text{-}to\text{-}peak}$) at the edge of the trap as shown in Figure 57. Thereafter, the inlet of the microfluidic channel was disconnected and the fluid in the device was evaporated for 5 hours at room temperature. The counter electrode of the dehydrated device was removed, a 10 nm of Au / Pd layer was deposited by sputtering (Desk II metal sputter / sample coater, Denton Vacuum, USA) on the surface of the device with nanoparticles attached. The devices with metal deposited on the surface were observed by scanning electron microscope (SEM, JSM-6460LV, JEOL Ltd. Japan). As shown in Figure 58, the 200 nm particles used in the trapping experiments were observed as single particles.

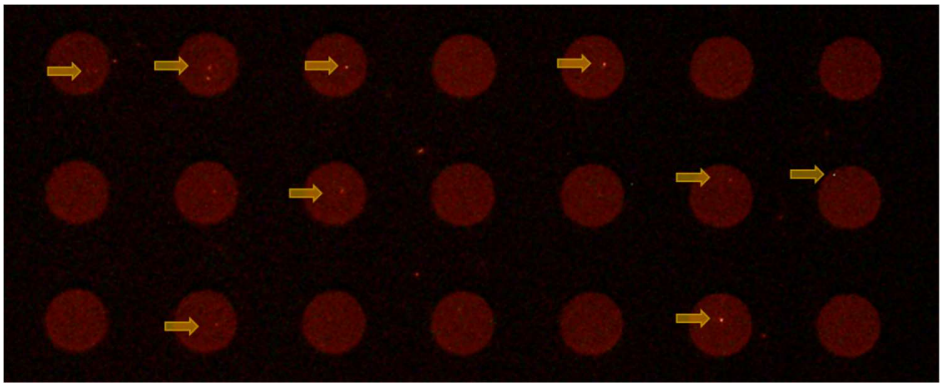

Figure 56. 200 nm particles trapped in the DEP trap by n-DEP.

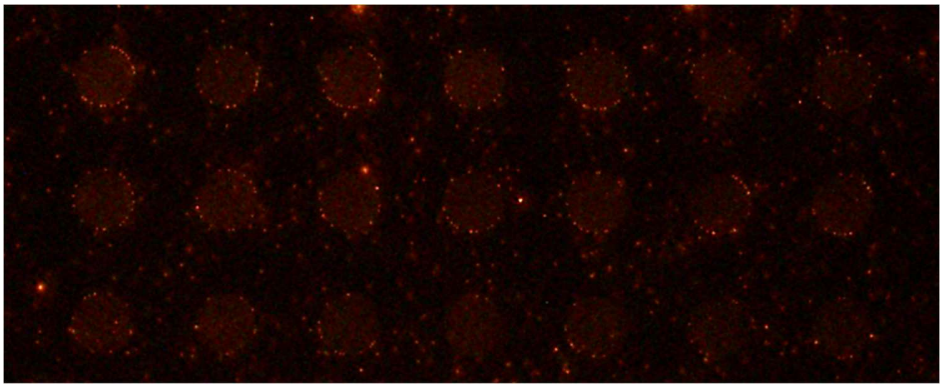

Figure 57. 200 nm particles trapped in the DEP trap by p-DEP.

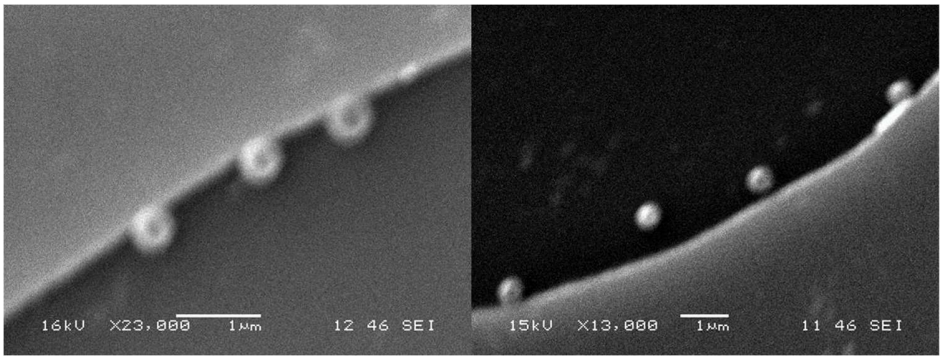

Figure 58. SEM images of 200 nm particles on the trap.

4.7 Selective single particles trapping among mixture

In order to evaluate whether the trap can selectively isolate and immobilize specific target particles in the mixture, selective single particle trapping experiment was performed. A mixture of 1, 2, and 3 μm radii polystyrene particles in the medium are flowing through the microchannels freely by the flow with no applied voltage on the trap electrodes as shown in Figure 59.

When the AC 1 MHz 8 Vpeak-to-peak of the electrical signal was applied on the trap electrodes, only the 2 μm particles around 400 μm/s velocities were captured in each trap by the negative DEP force as shown in Figure 60. Since the electric field distribution around each dielectrophoretic trap capturing a particle does not differ in the trap array, the same electrical and physical characteristics particles could be trapped in each trap under exact operation condition. After that, the AC electrical signals of the electrodes were removed, then trapped particles allowed the trap to escape. Thereafter, the flow rate of the mixture fluid in the microchannel was increased to about 650 μm/s, and the same AC electric signal was applied to the electrodes. At the increased flow rates, only 3 μm particles were successfully trapped as shown in Figure 61.

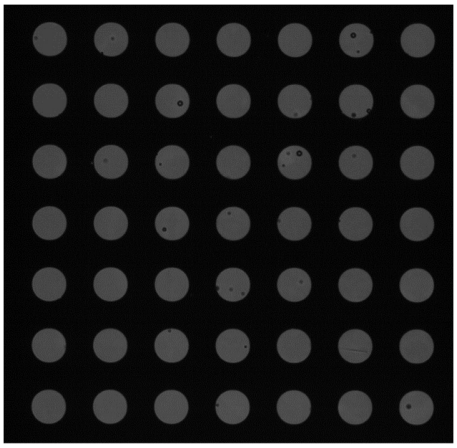

Figure 59. Flow of 1, 2 and 3 μm particle mixture when no voltage is applied.

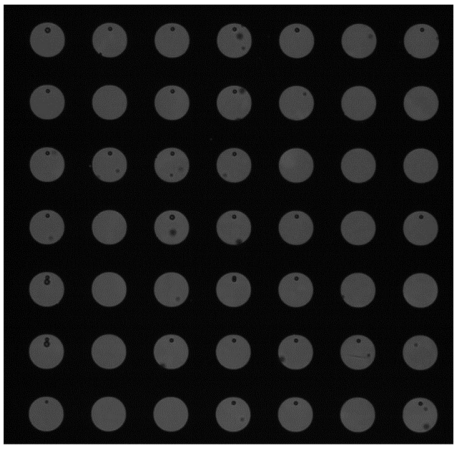

Figure 60. Isolation and immobilization of 2 μm particles.

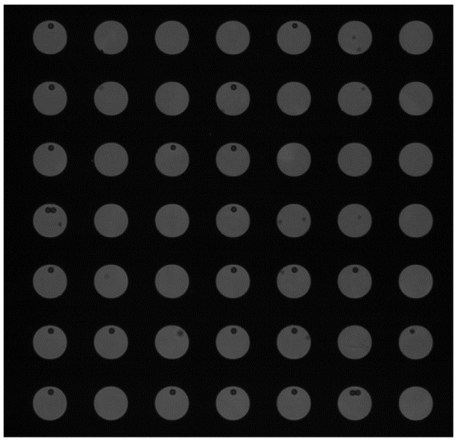

Figure 61. Isolation and immobilization of 3 μm particles.

Chapter 5

Conclusion

In this dissertation, a dielectrophoretic microfluidic trap device was developed and performed to separate and immobilize micro- and nano-particles in a single particle level. Based on the finite element analysis numerical simulation, the direction and amplitude of the dielectrophoretic force field were generated and the position of the trapped particles within the trap was evaluated according to the shape of the trap structure. An array of circular DEP traps enabled precise control of the electric force field by its symmetric and omnidirectional trapping properties. Trapping conditions such as the geometrical structure of the microchannel, particle velocity, particle size, and work required for targeted single particle trapping with optimal trapping efficiency were derived based on both numerical and experimental approaches. Using the developed microfluidic DEP trap device, the desired size particles from mixture were able to be isolated, trapped and immobilized.

The developed method to selectively trap the single particles and cells will enable further in-situ isolation and separation of the organelles from captured cells to perform various analysis related to biomedical applications. Moreover, the accomplishment of the study will significantly advance the separation and identification of single particles and molecules, such as DNA, by circumventing the drawbacks of current ensemble techniques which use the average of the massive number of events. Furthermore, multiple target objects can be analyzed in parallel by arranging traps into grid arrays, which is easily achieved by the photolithographic fabrication.

References

1. Huang LR, Cox EC, Austin RH, Sturm JC (2004) Continuous particle separation through deterministic lateral displacement. *Science*, 304(5673):987–990.

2. Ding X, Peng Z, Lin S-CS, Geri M, Li S, Li P, Chen Y, Dao M, Suresh S, Huang TJ (2014) Cell separation using tilted-angle standing surface acoustic waves. *Proceedings of the National Academy of Sciences*, 111(36):12992–12997.

3. Tauro BJ, Greening DW, Mathias RA, Ji H, Mathivanan S, Scott AM, Simpson RJ (2012) Comparison of ultracentrifugation, density gradient separation, and immunoaffinity capture methods for isolating human colon cancer cell line LIM1863-derived exosomes. *Methods*, 56(2):293–304. https://doi.org/10.1016/j.ymeth.2012.01.002

4. Merchant ML, Powell DW, Wilkey DW, Cummins TD, Deegens JK, Rood IM, McAfee KJ, Fleischer C, Klein E, Klein JB (2010) Microfiltration isolation of human urinary exosomes for characterization by MS. *PROTEOMICS - CLINICAL APPLICATIONS*, 4(1):84–96. https://doi.org/10.1002/prca.200800093

5. Böing AN, Pol E van der, Grootemaat AE, Coumans FAW, Sturk A, Nieuwland R (2014) Single-step isolation of extracellular vesicles by size-exclusion chromatography. *Journal of Extracellular Vesicles*, 3(0)https://doi.org/10.3402/jev.v3.23430

6. Bard MP, Hegmans JP, Hemmes A, Luider TM, Willemsen R, Severijnen L-AA, Meerbeeck JP van, Burgers SA, Hoogsteden HC, Lambrecht BN (2004) Proteomic Analysis of Exosomes Isolated from Human Malignant Pleural Effusions. *American Journal of Respiratory Cell and Molecular Biology*, 31(1):114–121. https://doi.org/10.1165/rcmb.2003-0238OC

7. Cantin R, Diou J, Bélanger D, Tremblay AM, Gilbert C (2008) Discrimination between exosomes and HIV-1: Purification of both vesicles from cell-free supernatants. *Journal of Immunological Methods*, 338(1–2):21–30. https://doi.org/10.1016/j.jim.2008.07.007

8. Chen C, Skog J, Hsu C-H, Lessard RT, Balaj L, Wurdinger T, Carter BS, Breakefield XO, Toner M, Irimia D (2010) Microfluidic isolation and transcriptome analysis of serum microvesicles. *Lab Chip*, 10(4):505–511. https://doi.org/10.1039/B916199F

9. Santana SM, Antonyak MA, Cerione RA, Kirby BJ (2014) Microfluidic isolation of cancer-cell-derived microvesicles from hetergeneous extracellular shed vesicle populations. *Biomedical Microdevices*, 16(6):869–877. https://doi.org/10.1007/s10544-014-9891-z

10. Chen C, Lin B-R, Wang H-K, Fan S-T, Hsu M-Y, Cheng C-M (2014) Paper-based immunoaffinity devices for accessible isolation and characterization of extracellular vesicles. *Microfluidics and Nanofluidics*, 16(5):849–856. https://doi.org/10.1007/s10404-014-1359-1

11. Wang Z, Wu H, Fine D, Schmulen J, Hu Y, Godin B, Zhang JXJ, Liu X (2013) Ciliated micropillars for the microfluidic-based isolation of nanoscale lipid vesicles. *Lab on a Chip*, 13(15):2879. https://doi.org/10.1039/c3lc41343h

12. Davies RT, Kim J, Jang SC, Choi E-J, Gho YS, Park J (2012) Microfluidic filtration system to isolate extracellular vesicles from blood. *Lab on a Chip*, 12(24):5202–5210. https://doi.org/10.1039/c2lc41006k

13. Lee K, Shao H, Weissleder R, Lee H (2015) Acoustic Purification of Extracellular Microvesicles. *ACS Nano*, 9(3):2321–2327. https://doi.org/10.1021/nn506538f

14. Qian C, Huang H, Chen L, Li X, Ge Z, Chen T, Yang Z, Sun L (2014) Dielectrophoresis for bioparticle manipulation. *International journal of molecular sciences*, 15(10):18281–18309.

15. Southern EM (1975) Detection of specific sequences among DNA fragments separated by gel electrophoresis. *Journal of molecular biology*, 98(3):503IN3509-508IN5517.

16. Harrison DJ, Manz A, Fan Z, Luedi H, Widmer HM (1992) Capillary electrophoresis and sample injection systems integrated on a planar glass chip. *Analytical chemistry*, 64(17):1926–1932.

17. Callewaert N, Contreras R, Mitnik-Gankin L, Carey L, Matsudaira P, Ehrlich D (2004) Total serum proteinN-glycome profiling on a capillary electrophoresis-microfluidics platform. *ELECTROPHORESIS*, 25(1819):3128–3131. https://doi.org/10.1002/elps.200406020

18. Park IS, Kwak TJ, Lee G, Son M, Choi JW, Choi S, Nam K, Lee S-Y, Chang W-J, Eom K, Yoon DS, Lee S, Bashir R, Lee SW (2016) Biaxial Dielectrophoresis Force Spectroscopy: A Stoichiometric Approach for Examining Intermolecular Weak Binding Interactions. *ACS Nano*, 10(4):4011–4019. https://doi.org/10.1021/acsnano.5b05286

19. Pohl HA (1978) Dielectrophoresis: The behavior of neutral matter in nonuniform electric field. *Cam bridge Cambridge UK*,

20. Dash S, Mohanty S (2014) Dielectrophoretic separation of micron and submicron particles: A review. *ELECTROPHORESIS*, 35(18):2656–2672. https://doi.org/10.1002/elps.201400084

21. Hughes MP, Morgan H, Rixon FJ (2002) Measuring the dielectric properties of herpes simplex virus type 1 virions with dielectrophoresis. *Biochimica et Biophysica Acta (BBA) - General Subjects*, 1571(1):1–8. https://doi.org/10.1016/S0304-4165(02)00161-7

22. Chan KL, Gascoyne PR, Becker FF, Pethig R (1997) Electrorotation of liposomes: verification of dielectric multi-shell model for cells. *Biochimica et Biophysica Acta (BBA)-Lipids and Lipid Metabolism*, 1349(2):182–196.

23. Kwak TJ, Lee JW, Yoon DS, Lee SW (2013) Investigation of the Binding Force between Protein A and Immunoglobulin G Using Dielectrophoretic (DEP) Tweezers Inside a Microfluidic Chip. *Journal of Biomedical Engineering Research*, 34(3):123–128.

24. Lee J, Kwak TJ, Yoon DS, Lee SW (2013) Characterization of Dielectrophoretic Force for the Structural Shapes of Window in Microfluidic Dielectrophoretic Chip. *Journal of Biomedical Engineering Research*, 34(4):189–196.

25. Kwak TJ, Lee H, Woehl JC, Chang W-J (2017) Dielectrophoretic particle trap to characterize the properties of single particle. *2017 IEEE Great Lakes Biomedical Conference (GLBC)*, :1–1. https://doi.org/10.1109/GLBC.2017.7928887

26. Lee H, Kwak TJ, Woehl JC, Chang W-J (2017) Numerical study of an array of dielectrophoretic traps to quantify physical properties of single particles. *2017 IEEE Great Lakes Biomedical Conference (GLBC)*, :1–1. https://doi.org/10.1109/GLBC.2017.7928877

27. Langer R, Vacanti J (1993) Tissue engineering. *Science*, 260(5110):920–926. https://doi.org/10.1126/science.8493529

28. El-Ali J, Sorger PK, Jensen KF (2006) Cells on chips. *Nature*, 442:403–411. https://doi.org/10.1038/nature05063

29. Bennett MR, Hasty J (2009) Microfluidic devices for measuring gene network dynamics in single cells. *Nature Reviews Genetics*, 10(9):628–638. https://doi.org/10.1038/nrg2625

30. Salafi T, Zeming KK, Zhang Y (2017) Advancements in microfluidics for nanoparticle separation. *Lab on a Chip*, 17(1):11–33. https://doi.org/10.1039/C6LC01045H

31. Yun C-K, Wook Hwang J, Joon Kwak T, Chang W-J, Ha S, Han K, Lee S, Choi Y-S (2019) Nanoinjection system for precise direct delivery of biomolecules into single cells. *Lab on a Chip*, 19(4):580–588. https://doi.org/10.1039/C8LC00709H

32. Dalili A, Samiei E, Hoorfar M (2019) A review of sorting, separation and isolation of cells and microbeads for biomedical applications: microfluidic approaches. *The Analyst*, 144(1):87–113. https://doi.org/10.1039/C8AN01061G

33. Zhang J, Yan S, Sluyter R, Li W, Alici G, Nguyen N-T (2014) Inertial particle separation by differential equilibrium positions in a symmetrical serpentine micro-channel. *Scientific Reports*, 4:4527. https://doi.org/10.1038/srep04527

34. Alejandro Hernández-Castro J, Li K, Meunier A, Juncker D, Veres T (2017) Fabrication of large-area polymer microfilter membranes and their application for particle and cell enrichment. *Lab on a Chip*, 17(11):1960–1969. https://doi.org/10.1039/C6LC01525E

35. Polniak DV, Goodrich E, Hill N, Lapizco-Encinas BH (2018) Separating large microscale particles by exploiting charge differences with dielectrophoresis. *Journal of Chromatography A*, 1545:84–92. https://doi.org/10.1016/j.chroma.2018.02.051

36. Chung C-C, Cheng I-F, Lin C-C, Chang H-C (2011) Rapid quantification of bio-particles based on image visualisation in a dielectrophoretic microfluidic chip. *Microfluidics and Nanofluidics*, 10(2):311–319. https://doi.org/10.1007/s10404-010-0670-8

37. Nieuwenhuis JH, Vellekoop MJ (2004) Simulation study of dielectrophoretic particle sorters. *Sensors and Actuators B: Chemical*, 103(1–2):331–338. https://doi.org/10.1016/j.snb.2004.04.062

38. Pesch GR, Lorenz M, Sachdev S, Salameh S, Du F, Baune M, Boukany PE, Thöming J (2018) Bridging the scales in high-throughput dielectrophoretic (bio-)particle separation in porous media. *Scientific Reports*, 8(1)https://doi.org/10.1038/s41598-018-28735-w

39. Rosenthal A, Voldman J (2005) Dielectrophoretic Traps for Single-Particle Patterning. *Biophysical Journal*, 88(3):2193–2205. https://doi.org/10.1529/biophysj.104.049684

40. Nestor BA, Samiei E, Samanipour R, Gupta A, Van den Berg A, Leon Derby MD de, Wang Z, Nejad HR, Kim K, Hoorfar M (2016) Digital microfluidic platform for dielectrophoretic patterning of cells encapsulated in hydrogel droplets. *RSC Advances*, 6(62):57409–57416.

41. P. Macdonald N, Menachery A, Reboud J, M. Cooper J (2018) Creating tissue on chip constructs in microtitre plates for drug discovery. *RSC Advances*, 8(18):9603–9610. https://doi.org/10.1039/C8RA00849C

42. Pohl HA, Hawk I (1966) Separation of Living and Dead Cells by Dielectrophoresis. *Science*, 152(3722):647–649. https://doi.org/10.1126/science.152.3722.647-a

43. Hu X, Bessette PH, Qian J, Meinhart CD, Daugherty PS, Soh HT (2005) Marker-specific sorting of rare cells using dielectrophoresis. *Proceedings of the National Academy of Sciences*, 102(44):15757–15761. https://doi.org/10.1073/pnas.0507719102

44. Ibsen SD, Wright J, Lewis JM, Kim S, Ko S-Y, Ong J, Manouchehri S, Vyas A, Akers J, Chen CC, Carter BS, Esener SC, Heller MJ (2017) Rapid Isolation and Detection of Exosomes and Associated Biomarkers from Plasma. *ACS Nano*, 11(7):6641–6651. https://doi.org/10.1021/acsnano.7b00549

45. Dittrich PS, Manz A (2006) Lab-on-a-chip: microfluidics in drug discovery. *Nature Reviews Drug Discovery*, 5(3):210–218. https://doi.org/10.1038/nrd1985

46. Ivanoff CS, Hottel TL, Garcia-Godoy F (2012) Dielectrophoresis: A model to transport drugs directly into teeth. *ELECTROPHORESIS*, 33(8):1311–1321. https://doi.org/10.1002/elps.201100505

47. Pethig R (2013) Dielectrophoresis: An assessment of its potential to aid the research and practice of drug discovery and delivery. *Advanced Drug Delivery Reviews*, 65(11):1589–1599. https://doi.org/10.1016/j.addr.2013.09.003

48. Ibsen Stuart, Sonnenberg Avery, Schutt Carolyn, Mukthavaram Rajesh, Yeh Yasan, Ortac Inanc, Manouchehri Sareh, Kesari Santosh, Esener Sadik, Heller Michael J. (2015) Recovery of Drug Delivery Nanoparticles from Human Plasma Using an Electrokinetic Platform Technology. *Small*, 11(38):5088–5096. https://doi.org/10.1002/smll.201500892

49. Pethig R (2017) Review—Where Is Dielectrophoresis (DEP) Going? *Journal of The Electrochemical Society*, 164(5):B3049–B3055. https://doi.org/10.1149/2.0071705jes

50. Dunn SE, Brindley A, Davis SS, Davies MC, Illum L (1994) Polystyrene-Poly (Ethylene Glycol) (PS-PEG2000) Particles as Model Systems for Site Specific Drug Delivery. 2. The Effect of PEG Surface Density on the in Vitro Cell Interaction and in VivoBiodistribution. *Pharmaceutical Research*, 11(7):1016–1022. https://doi.org/10.1023/A:1018939521589

51. Lunov O, Syrovets T, Loos C, Beil J, Delacher M, Tron K, Nienhaus GU, Musyanovych A, Mailänder V, Landfester K, Simmet T (2011) Differential Uptake of Functionalized Polystyrene Nanoparticles by Human Macrophages and a Monocytic Cell Line. *ACS Nano*, 5(3):1657–1669. https://doi.org/10.1021/nn2000756

52. Tenzer S, Docter D, Kuharev J, Musyanovych A, Fetz V, Hecht R, Schlenk F, Fischer D, Kiouptsi K, Reinhardt C, Landfester K, Schild H, Maskos M, Knauer SK, Stauber RH (2013) Rapid formation of plasma protein corona critically affects nanoparticle pathophysiology. *Nature Nanotechnology*, 8(10):772–781. https://doi.org/10.1038/nnano.2013.181

53. R Development Core Team (2008) R: A Language and Environment for Statistical Computing. http://www.R-project.org

54. Wood SN (2017) Generalized Additive Models: An Introduction with R.

55. Zhao Y, Sam Lai HS, Zhang G, Lee G-B, Jung Li W (2014) Rapid determination of cell mass and density using digitally controlled electric field in a microfluidic chip. *Lab on a Chip*, 14(22):4426–4434. https://doi.org/10.1039/C4LC00795F

56. Marki A, Ermilov E, Zakrzewicz A, Koller A, Secomb TW, Pries AR (2014) Tracking of fluorescence nanoparticles with nanometre resolution in a biological system: assessing local viscosity and microrheology. *Biomechanics and Modeling in Mechanobiology*, 13(2):275–288. https://doi.org/10.1007/s10237-013-0499-7

57. Nasse MJ, Woehl JC (2010) Realistic modeling of the illumination point spread function in confocal scanning optical microscopy. *JOSA A*, 27(2):295–302. https://doi.org/10.1364/JOSAA.27.000295

58. Richardson WH (1972) Bayesian-Based Iterative Method of Image Restoration$\ast$. *J. Opt. Soc. Am.*, 62(1):55–59. https://doi.org/10.1364/JOSA.62.000055

59. Lucy LB (1974) An iterative technique for the rectification of observed distributions. *The astronomical journal*, 79:745.

60. Dey N, Blanc-Feraud L, Zimmer C, Roux P, Kam Z, Olivo-Marin J-C, Zerubia J (2006) Richardson–Lucy algorithm with total variation regularization for 3D confocal microscope deconvolution. *Microscopy research and technique*, 69(4):260–266.

61. Sage D, Donati L, Soulez F, Fortun D, Schmit G, Seitz A, Guiet R, Vonesch C, Unser M (2017) DeconvolutionLab2: An open-source software for deconvolution microscopy. *Methods*, 115:28–41.

62. Son M, Choi S, Ko KH, Kim MH, Lee S-Y, Key J, Yoon Y-R, Park IS, Lee SW (2016) Characterization of the Stiffness of Multiple Particles Trapped by Dielectrophoretic Tweezers in a Microfluidic Device. *Langmuir*, 32(3):922–927. https://doi.org/10.1021/acs.langmuir.5b03677

63. Cox RG, Brenner H (1967) The slow motion of a sphere through a viscous fluid towards a plane surface—II Small gap widths, including inertial effects. *Chemical Engineering Science*, 22(12):1753–1777. https://doi.org/10.1016/0009-2509(67)80208-2

Curriculum Vitae

Tae Joon Kwak

Education

Ph.D., Mechanical Engineering, Minor in Biomedical Engineering August 2019

University of Wisconsin-Milwaukee Milwaukee, WI

• Dissertation title: "Investigation of Dielectrophoretic Microfluidic Trap System for Separation and Parallel Analysis of Single Particles"

Master of Science in Biomedical Engineering February 2014

Yonsei University Seoul, South Korea

• Thesis title: "Development of Lateral Dielectrophoresis Force Spectroscopy"

Bachelor of Engineering in Oriental Biomedical Engineering February 2011

Sangji University Wonju, South Korea

Research experience

Research Assistant January 2015 – August 2019

Biosensor and BioMEMS Laboratory, University of Wisconsin-Milwaukee Milwaukee, WI

• Designed and developed microfluidic particle separation system

• Designed and developed microfluidic point-of-care (POC) biosensor device for fluid characterization

• Devised fabrication technique of three-dimensional flow paper-fluidic analytical devices (μ-PADs)

• Performed modeling and simulation of microfluidic devices by COMSOL finite element analysis (FEA)

• Designed microfluidic mixers and analyzed fluidic behavior

Research Assistant March 2011 – May 2014

Nano Bio System Research Laboratory, Yonsei University Wonju, South Korea

• Designed and developed microfluidic intermolecular force spectroscopy system

• Performed thin film and bioassay surface characterization with AFM, SEM

• Performed COMSOL FEA modeling for electric potential, field and thermal effect of microfluidic devices

Undergraduate Research Assistant March 2009 – February 2011

Nano-Bio Laboratory, Sangji University Wonju, South Korea

• Performed electromagnetic multilayer thin film device fabrication

• Performed COMSOL FEA modeling of magnetic field effect on human body for electric vehicle development

Undergraduate Research Assistant September 2005 – January 2007

Nano-Bio Laboratory, Sangji University Wonju, South Korea

• Analyzed of magnetic properties in Nano-materials using spin valve MEMS sensor

• Performed thin film fabrication

Teaching and advising experience

Teaching Assistant

University of Wisconsin-Milwaukee August 2018 – May 2019

• Engineering Fundamentals II, Spring 2019
  - Discussed tenets of design, project implementation for engineering problem solving
  - Instructed engineering visualization, technical communication, and data collection and analysis
  - Instructed computerized parametric 3D modeling software with PTC Creo (Pro/E)

• Mechanical Engineering Experimentation, Fall 2018, Spring 2019 (Part)
  - Discussed design of experiments (DOE) and experimental methods for engineering problem solving
  - Instructed use of hands-on mechanical and electrical measurement tools
  - Taught measurement of basic quantities, statistical data analysis, dynamic response of instruments
  - Instructed computerized experiment based on data acquisition systems with LabVIEW

Teaching Assistant

Yonsei University September 2012 – July 2013

• Application of Bio-MEMS, Spring 2013
  - Taught fundamentals of MEMS, microelectronic fabrication, process integration
  - Instructed semiconductor manufacturing process such as photolithography, CVD, PVD, measurement
  - Instructed MEMS analysis using COMSOL Multiphysics finite element analysis software

• Practice in Medical Engineering, Fall 2012
  - Instructed fundamentals of electronics, mechanical engineering
  - Taught principle and characteristics of medical device, how to use measuring device
  - Discussed about medical safety, regulation and information

Student advised

University of Wisconsin-Milwaukee January 2015 – August 2019

• Supported for Undergraduate Research Fellows (SURF) program
  - Provided advice to five undergrad students to learn microfluidic sensor fabrication processes, fluidic flow generation, research skills, analytical methods

• Provided advice to two graduate students
  - Microelectromechanical system fabrication processes
  - Microfluidic sensor fabrication processes
  - Finite element analysis method design and simulation

• Provided advice to one high school student
  - Microelectromechanical system fabrication processes

Student advised

Yonsei University June 2011 – August 2013

• Supported for Women In Science, Engineering and Technology (WISET) program
  - Taught twelve high school students to learn semiconductor fabrication processes, lab equipment, experimental process, data analysis

Honors and Awards

- **CEAS Academic Excellence Award**, University of Wisconsin-Milwaukee May 2019
  - Awarded at a CEAS order of engineer graduation ceremony to a graduating student who has achieved exceptional academics, demonstrated outstanding research, and extra-curricular accomplishments at UWM.

- **Third Place Graduate Award**, UWM CEAS Research Poster Competition May 2019
  - Related publication: Rahman, MRU, **Kwak, TJ**., Woehl, JC., Chang, W-J., "Numerical study on the effect of dielectrophoretic single particle trap geometry", UWM CEAS Research Poster Competition, Milwaukee, WI; 04/2019

- **Distinguished Dissertation Fellowship award**, University of Wisconsin-Milwaukee September 2018
  - The Distinguished Dissertation Fellowship (DDF) award recognizes and supports the most academically excellent Ph.D. students who have achieved dissertator status at UW-Milwaukee. The fellowship stipend is $16,500 and $1,000 travel award with full tuition coverage.

- Finalist at **Mike Krauski Memorial Award**, UW-Milwaukee student research poster completion April 2018
  - One of three finalist at Mike Krauski Memorial Award from UW-Milwaukee student research poster completion.

- **Chancellor's Graduate Student Award**, University of Wisconsin-Milwaukee February 2018
  - The Chancellor's Graduate Student Award is contingent upon the student's continuation in good standing in graduate program. (Award: $515)

- **Asian Faculty and Staff Association Honorary Award**, University of Wisconsin-Milwaukee November. 2017
  - The Asian Faculty and Staff Association (AFSA) Award recognizes outstanding Asian and Asian American students for their academic excellence, as well as their commitment and contribution to the Asian community. Only two graduate students and one undergraduate student are awarded annually. (Award: $200)

- **Distinguished Graduate Student Fellowship award**, University of Wisconsin-Milwaukee October. 2017
  - The Distinguished Graduate Student Fellowship (DGSF) recognizes and supports the most academically excellent master's and doctoral students enrolled at UW-Milwaukee. The fellowship stipend is $15,000 and $1,000 travel award with full tuition coverage.

- **Chancellor's Graduate Student Award**, University of Wisconsin-Milwaukee February 2017
  - The Chancellor's Graduate Student Award is contingent upon the student's continuation in good standing in graduate program. (Award: $1,500)

- **The people who have brought great honor to Korea**, Biological Research Information Center March 2016
  - Honors awarded to Korean scientists who published to the world's most authoritative journals of life sciences as the first author or corresponding author. (Related paper: Park, IS., **Kwak, TJ.(Co-1st Author)**, Lee, G., Son, M., Choi, JW., Choi, S., Nam, K., Lee, S-Y., Chang, W-J., Eom, K., Yoon, DS., Lee, S., Bashir, R., Lee, SW., "Biaxial Dielectrophoresis Force Spectroscopy: A Novel Stoichiometric Approach for Examining Intermolecular Weak Binding Interactions", ACS Nano, 2016, 10, 4011-4019, IF=13.942).

- **College of Engineering & Applied Science Dean's Scholarship award**, UW-Milwaukee May 2015
  - One of three award recipient. (Award: $650)
- **Third Place Graduate Award**, IEEE Larry Hause Poster Competition May 2015
  - Related publication: Francis, A., Udad, X., **Kwak, TJ.**, Bergren, R., Woehl, JC., Chang, W-J., Avdeev, I., "Novel Molecular Trapping Technology and Translational Prototype Development", IEEE-USA Annual Meeting 2015 and 36th Great Lakes Biomedical Conference; Milwaukee Hilton City Center, Milwaukee, WI, 05/14/2015.
- **Academic Achievement**, Brain Korea (BK) 21 at Yonsei University Dec. 2012
  - Awarded to a student who demonstrated outstanding research and exceptional academics. (Award: $3,000)
- **Academic Achievement**, Brain Korea (BK) 21 at Yonsei University Nov. 2011
  - Awarded to a student who demonstrated outstanding research and exceptional academics. (Award: $3,000)
- **Academic Achievement**, Brain Korea (BK) 21 at Yonsei University Jun. 2011
  - Awarded to a student who demonstrated outstanding research and exceptional academics. (Award: $3,000)
- **Second place high Honors**, Sangji University February 2010
  - Awarded to a student who has achieved exceptional academics. The fellowship covered 50% of tuition fees.
- **First place high Honors**, Sangji University February 2006
  - Awarded to a student who has achieved exceptional academics. The fellowship covered 80% of tuition fees.
- **First place high Honors**, Sangji University August 2005
  - Awarded to a student who has achieved exceptional academics. The fellowship covered 80% of tuition fees.

Publications

Articles and papers published in academic and professional print and electronic journals

1. **Kwak, TJ.,** Lee, H., Lee, SW., Woehl, JC., Chang, W-J., "Selective isolation of the specific size moving particles", (Manuscript in preparation)
2. **Kwak, TJ.,** Hossen, I., Chang, W-J., Lee, CH., "Localized dielectric loss heating in dielectrophoresis devices", (Manuscript in preparation)
3. **Kwak, TJ.,** Jung, HH., Stanisic, G., BD Allen., Chang, W-J., M Demirel, "Characterization and separation of synthesized protein particles", (Manuscript in preparation)
4. **Kwak, TJ.,** Rahman, MRU., Chang, W-J., "Characterization of the behavior of single particle for the Geometry of trap electrode in microfluidic dielectrophoretic trap", (Manuscript in preparation)
5. Ryu, M., Rahman, MRU., **Kwak TJ.,** Gunasekaran, S., Chang, W-J., "Low-cost phosphate sensor: Low interference high-sensitive phosphate sensing structure, optimize configuration", (Manuscript in preparation)
6. Mehrnezhad, A., **Kwak, TJ**., Kim, S., Chang, W-J., Park, K., "Moving shot, an affordable and high-throughput setup for direct imaging of fast-moving microdroplets", Microsystem Technologies, 2019, Online First Articles, (IF=1.581)

7. Yun, C-K., Hwang, JW., **Kwak, TJ**., Chang, W-J., Han, K., Lee, S. and Choi, Y-S., "Nanoinjection System for Precise Direct Delivery of Large Molecules into Single Cells", Lab on a Chip, 2019, 19, 580-588, **(Cover article, IF=5.995)**
8. **Kwak, TJ**., Kwon, W., Yang, J., Lee, SW., Chang, W-J., "Rapid fabrication of versatile omni-directional and long-distance three-dimensional flow paper-fluidic analytical devices using cut-and-insert method for biomedical applications", Analytical Methods, 2018, 10, 4648-4654, (IF=2.073)
9. Yang, J., **Kwak, TJ**., Zhang, X., McClain, R., Chang, W-J., Gunasekaran, S., "Iridium oxide-reduced graphene oxide hybrid thin film modified screen-printed electrode as disposable electrochemical paper microfluidic pH sensor", Journal of Visualized Experiments, 2016, 117, e53339, (IF=1.113)
10. **Kwak, TJ**., Nam, YG., Najera, MA., Lee, SW., Strickler, JR., Chang, W-J., "Convex Grooves in Staggered Herringbone Mixer Improve Mixing Efficiency of Laminar Flow in Microchannel", PLoS ONE, 2016, 11(11), e0166068, (IF=2.806)
11. Yang, J., **Kwak, TJ**., Zhang, X., McClain, R., Chang, W-J., Gunasekaran, S., "Digital pH test strips for in-field pH monitoring using iridium oxide-reduced graphene oxide hybrid thin films", ACS Sensors, 2016, 1(10), 1235-1243, **(IF=5.711)**
12. Park, IS., **Kwak, TJ.(Co-1st Author)**, Lee, G., Son, M., Choi, JW., Choi, S., Nam, K., Lee, S-Y., Chang, W-J., Eom, K., Yoon, DS., Lee, S., Bashir, R., Lee, SW., "Biaxial Dielectrophoresis Force Spectroscopy: A Novel Stoichiometric Approach for Examining Intermolecular Weak Binding Interactions", ACS Nano, 2016, 10, 4011-4019, **(IF=13.942)**
13. Lee, W., Jung, H., Son, M., Lee, H., **Kwak, TJ**., Lee, G., Kim, CH., Lee, SW., and Yoon, DS., "Characterization of the regrowth behavior of amyloid-like fragmented fibrils decomposed by ultrasonic treatment", RSC Advances, 2014, 4(100), 56561-56566, (IF=3.840)
14. Lee, JW., **Kwak, TJ**., Yoon, DS., Lee, SW., "Characterization of Dielectrophoretic Force for the Structural Shapes of Window in Microfluidic Dielectrophoretic Chip", Journal of Biomedical Engineering Research, 2013, 34(4), 189-196
15. **Kwak, TJ**., Lee, JW., Yoon, DS., Lee, SW., "Investigation of the Binding Force between Protein A and Immunoglobulin G Using Dielectrophoretic (DEP) Tweezers Inside a Microfluidic Chip", Journal of Biomedical Engineering Research, 2013, 34(3), 123-128
16. Choi, J-G., **Kwak, TJ**., Lee, S-S., Sim, J-T., "Shape Magnetic Anisotropy on Magnetic Easy Axis of NiFe/Cu/NiFe/IrMn Spin Valve Thin Film", Journal of the Korean Magnetics Society, 04/2010; 20(2):35-40

Papers and presentations at academic and professional meetings

1. **Kwak, TJ**., Woehl, JC., Chang, W-J., "Dielectrophoretic particle trap: novel manipulation and analysis technique at the single particle level", UWM CEAS Research Poster Competition, Milwaukee, WI; 04/2019
2. Rahman, MRU, **Kwak, TJ**., Woehl, JC., Chang, W-J., "Numerical study on the effect of dielectrophoretic single particle trap geometry", UWM CEAS Research Poster Competition, Milwaukee, WI; 04/2019

3. Yun, C-K., Rahman, MUR., **Kwak, TJ.**, Chang, W-J., Choi, Y-S., "Dielectrophoretic particle separation for organelle isolation and analysis from the single cell", The American Society for Cell Biology (ASCB) and European Molecular Biology Organization (EMBO) 2018 meeting, San Diego, CA; 12/10/2018
4. **Kwak, TJ**., Woehl, JC., Chang, W-J., "Dielectrophoretic Corral Trap for Single Particle Trapping and Characterization Technique", Biomedical Engineering Society (BMES) 2018, Atlanta, GA; 10/18/2018
5. **Kwak, TJ**., Woehl, JC., Chang, W-J., "Dielectrophoretic particle trap: novel trapping and analysis technique at single particle level", UWM CEAS Research Poster Competition, Milwaukee, WI; 04/2018
6. **Kwak, TJ**., Lee, H., Woehl, JC., Chang, W-J., "Dielectrophoretic particle trap to characterize the properties of single particle", 2017 IEEE Great Lakes Biomedical Conference (GLBC), Milwaukee, WI, 2017, pp. 1-1
7. Lee, H., **Kwak, TJ**., Woehl, JC., Chang, W-J., "Numerical study of an array of dielectrophoretic traps to quantify physical properties of single particles", 2017 IEEE Great Lakes Biomedical Conference (GLBC), Milwaukee, WI, 2017, pp. 1-1
8. **Kwak, TJ.,** Lee, H., Woehl, JC., Chang, W-J., "Single particle trapping and characterization using dielectrophoretic particle trap", UWM CEAS Research Poster Competition, Milwaukee, WI; 04/2017
9. Lee, H., **Kwak, TJ**., Woehl, JC., Chang, W-J., "Numerical simulation of the force field distribution in an array of circular dielectrophoresis traps", UWM CEAS Research Poster Competition, Milwaukee, WI; 04/2017
10. **Kwak, TJ**., Nam, YG., Najera, MA., Lee, SW., Strickler, JR., Chang, W-J., "Improved Mixing Efficiency Using Convex Grooves in Passive Micro-mixer With Low Reynolds Number Scheme", Biomedical Engineering Society (BMES) 2016, Minneapolis, MN; 10/07/2016
11. **Kwak, TJ**., Nam, YG., Strickler, JR., Chang, W-J., "Improved mixing efficiency using Convex Grooves in passive micro-mixer with low Reynolds number scheme", UWM CEAS Research Poster Competition, Milwaukee, WI; 04/23/2016
12. Francis, A., Udad, X., **Kwak, TJ**., Bergren, R., Woehl, JC., Chang, W-J., Avdeev, I., "Novel Molecular Trapping Technology and Translational Prototype Development", IEEE-USA Annual Meeting 2015 and 36th Great Lakes Biomedical Conference; Milwaukee Hilton City Center, Milwaukee, WI; 05/14/2015. (IEEE Larry Hause Student Poster Competition 2015 3rd Place Graduate Award)
13. Park, IS., **Kwak, TJ**., Yoon, DS., Lee, SW., "Dielectrophoresis Force Spectroscopy for defining the directional effect of intermolecular bonds", The Korean MEMS Conference 2015; 04/02/15
14. Lee, W., Jung, H., **Kwak, TJ**., Son, M., Lee, G., Lee, SW., Yoon, DS., "Surface Potential Characterization of Regrown Amyloid-Like Fibrils via Kelvin Probe Force Microscopy", Materials Research Society (MRS) Fall Meeting & Exhibit, Boston, MA; 12/2014.
15. Lee, W., Lee, H., Jung, H., Son, M., **Kwak, TJ**., Lee, G., Lee, SW., Yoon, DS., "Surface Potential Characterization of Regrown Amyloid Fibrils Originated from Fragments by Ultrasonic Treatment", International BioMedical Engineering Conference (IBEC); 11/2014

16. Park, IS., Lee, JW., Lee, G., Lee, TW., **Kwak, TJ**., Kim, HS., Lee, SY., Yoon, DS., Lee, SW., "Dielectrophoretic On-Chip for Simultaneous Detection of Live Cell Responses to Small Molecule Drugs", 2014 Annual Fall Meeting of The BioChip Society; 09/2014
17. Lee, W., Jung, H., **Kwak, TJ**., Son, M., Lee, G., Lee, SW., Yoon, DS., "Mapping the surface potential rejoined protein fibrils", 2014 Annual Fall Meeting of The BioChip Society; 09/2014
18. **Kwak, TJ**., Choi, B., Chang, W-J., Yoon, DS., Lee, SW., "Investigation of lateral dielectrophoresis force spectroscopy", 7th Asia-pacific Conference on Transducers and Micro/nano Technologies (APCOT); 06/2014
19. **Kwak, TJ**., Choi, S., Choi, B., Son, M., Lee, SW., "Investigation of the binding force between Protein A and Immunoglobulin G using dielectrophoretic tweezers inside a microfluidic device", The Korea Society of Medical & Biological Engineering 2014 May 049; 05/2014
20. **Kwak, TJ**., Choi, B., Choi, S., Yoon, DS., Lee, SW., "Investigation of lateral dielectrophoresis force spectroscopy", The Korea Society of Medical & Biological Engineering 2014 May 049; 05/2014
21. Lee, W., Jung, H., **Kwak, TJ**., Son, M., Lee, G., Lee, SW., Yoon, DS., "Decomposition of Protein Fibrils by Ultrasonic Energy", The Korea Society of Medical & Biological Engineering 2014 May 049; 05/2014
22. **Kwak, TJ**., Choi, S., Choi, B., Lee, SW., "Investigation of the binding force between Protein A and Immunoglobulin G using dielectrophoretic tweezers inside a microfluidic device", 2014 Annual Spring Meeting of The BioChip Society; 04/2014
23. **Kwak, TJ**., Choi, B., Choi, S., Chang, W-J., Yoon, DS., Lee, SW., "Investigation of lateral dielectrophoresis force spectroscopy", 2014 Annual Spring Meeting of The BioChip Society; 04/2014
24. **Kwak, TJ**., Lee, SW., "Microfluidic Multifunctional Probe Array Dielectrophoretic Force Spectroscopy (MDFS) with Lateral DEP force", 2013 Annual Spring Meeting of The BioChip Society; 05/2013
25. **Kwak, TJ**., Insu Park, Choi, B., Lee, JW., Lee, SW., "Application of Microfluidic Multifunctional Probe Array Dielectrophoretic Force Spectroscopy with Lateral DEP force", 15th The Korean MEMS Conference 2013; 04/2013
26. Lee, JW., Lee, TW., **Kwak, TJ**., Choi, B., Lee, SW., "Dielectrophoretic technique for classifying the micro size cells", 2012 Annual Fall Meeting of The BioChip Society; 10/2012
27. Lee, JW., Lee, TW., **Kwak, TJ**., Choi, B., Lee, SW., "Dielectrophoretic technique for classifying the cell and measurement of mechanical characteristic of cell", 2012 Annual Spring Meeting of The BioChip Society; 05/2012
28. Lee, JW., Park, IS., **Kwak, TJ**., Choi, B., Eom, KH., Kwon, TY., Yoon, DS., Lee, SW., "Dielectrophoretic technique for classifying of physical characteristic of cell", The Korea Society of Medical & Biological Engineering 2011 Nov 44; 11/2011
29. Park, IS., **Kwak, TJ**., Choi, B., Son, JS., Eom, KH., Kwon, TY., Yoon, DS., Lee, SW., "Multifunctional Probe Array Dielectrophoretic Force Spectroscopy in a microfluidic device", Korea Society of Medical & Biological Engineering 2011 Nov 44; 11/2011

30. Lee, JW., **Kwak, TJ**., Choi, B., Eom, KH., Kwon, TY., Yoon, DS., Lee, SW., "Dielectrophoretic technique for classifying of physical characteristic of cell", 2011 Annual Fall Meeting of The BioChip Society; 11/2011
31. Park, IS., **Kwak, TJ**., Choi, B., Lee, JW., Eom, KH., Kwon, TY., Yoon, DS., Lee, SW., "Multifunctional Probe Array Dielectrophoretic Force Spectroscopy in a microfluidic device", 2011 Annual Fall Meeting of The BioChip Society; 11/2011
32. Park, IS., **Kwak, TJ**., Choi, B., Lee, JW., Eom, KH., Kwon, TY., Yoon, DS., Lee, SW., "Dielectrophoretic Tweezers inside a Microfluidic Device for measurement of Hydrogen bond", The Korea Society of Medical & Biological Engineering 2011 May 43; 05/2011
33. Choi, J-G., Sim, J-T., **Kwak, TJ**., Son, I-H., Hwang, D-G., Rhee, J-R., Lee, S-S., "Magnetic Properties of Two-layered Ferromagnetic Films with a Conetic Intermediately Super-soft Magnetic Layer of Different Thickness", Proceedings of the Korean Magnetics Society Conference 2010, (6), 148-150
34. An, M-C., Kim, M-S., Choi, S-D., Yu, H-J., **Kwak, TJ**., Kim, S-U., Hwang, D-G., Lee, S-S., "Detection of magnetic properties in nano-particle and human blood using spin valve bio sensor", Proceedings of the Korean Magnetics Society Conference 2006, (6), 148-149
35. Choi, S-D., Kim, S-U., Ju, H-W., An, M-C., Kim, M-S., **Kwak, TJ**., Choi, J-H., Kim, H-S., Yun, D-G., Heo, J., Baek, J-Y., Kim, J-G., Lee, G-A., "The contamination effect of MgO sputter in [Pd/Co] multi-layer film", Proceedings of the Korean Magnetics Society Conference 2006, (6), 138-139
36. Exhibition: "Pulse Wave diagnostor" and "Tongues condition diagnostor", Korea International Medical Hospital Equipment Show (KIMES), March 2010

Intellectual properties

Patent

1. Sang Woo Lee, Wonseok Lee, Hyungbeen Lee, Choi, S.,Myounggu Son, Gyudo Lee, Tae Joon Kwak, Dae Sung Yoon, "Method for decomposition or regrowth in axial direction of amyloid fibrils by ultra-sonication", application number: 10-2015-0017641, 2015, Korea
2. Sang Woo Lee, Tae Joon Kwak, Park, IS., Choi, S.,Myounggu Son, Kihwan Nam, Bumjoon Choi, "Method for measurement of biomolecular binding forces using lateral dielectrophoresis force spectroscopy", application number: 10-2014-0038426, 2014, Korea
3. Sang Woo Lee, Tae Joon Kwak, Park, IS., Choi, S.,Myounggu Son, Kihwan Nam, Bumjoon Choi, "Lateral dielectrophoresis force spectroscopy for the measurement of bimolecular binding forces", application number: 10-2014-0023514, 2014, Korea
4. Sang Suk Lee, Jung Ho Ahn, Tae Joon Kwak, "Stimulate acupuncture spots using portable sound device", application number, 10-2010-0127706, 2010, registration number: 10-1236365, 2013, Korea

Invention pre-disclosures

1. Woo-Jin Chang, Tae Joon Kwak, Hwangjae Lee, Jörg C. Woehl, Dielectrophoretic trap for efficient separation and patterning of single particles, IP-0026, March 2019.
2. Woo-Jin Chang, Tae Joon Kwak, Hwangjae Lee, Jörg C. Woehl, Single particle manipulation system using dielectrophoresis (DEP) trap and DC-offset for quantitation of cell motility, IP-1537, February 2017.
3. Woo-Jin Chang, Tae Joon Kwak, Continuous electrical extracellular vesicles separation system, IP-1497, March 2016.
4. Woo-Jin Chang, Tae Joon Kwak, Wookkun Kwon, Rapid fabrication of three-dimensional flow paper-fluidic device by using novel cut-and-insert method, IP-1464, June 2015.
5. Woo-Jin Chang, Tae Joon Kwak, Jörg C. Woehl, Dielectrophoretic chromatography system for rapid separation of bioparticles, IP-1587, Jan 2018

Professional Activities

- Member: Biomedical engineering society (BMES) 2016-2019
- Member: The Korean BioChip Society (KBCS) 2014-2015
- Member: The Society of Micro and Nano Systems 2013-2014
- Member: The Korean society of medical and biological engineering (KOSOMBE) 2011-2014

Skills

Fabrication

• Photo Lithography, Sputtering, Milling, Chemical vapor deposition, Thermal evaporation, Spin coating, E-beam evaporation, UV aligning, Wet etch, Plasma etch, Spin coating, 3D printing

Material and Surface Analysis

• Scanning electron microscope (SEM), Atomic force microscope (AFM), 3D laser confocal microscope, Zeta potential, Fourier-transform infrared spectroscopy (FTIR)

Numerical and Finite Element Analysis (FEA)

• COMSOL Multiphysics, ANSYS, MATLAB

Designing and Engineering Software

• AutoCAD, PTC Creo (Pro/E), Sketchup, LabVIEW

Flow Control

• Dolomite pump, Syringe pump

Statistical Analysis

• Origin Lab, Excel, R

Cell culture

• Mammalian cell culture